Published in final edited form as:
Top Magn Reson Imaging. 2010 October ; 21(5): 275–289. doi:10.1097/RMR.0b013e31823ccebc.

Conventional and Ultrashort MRI of Articular Cartilage, Meniscus and Intervertebral Disc

Won C. Bae, Ph.D.[1] **[Assistant Professor]**, **Jiang Du, Ph.D.**[1] **[Associate Professor]**, **Graeme M. Bydder, M.B., Ch.B.**[1] **[Professor]**, and **Christine B. Chung, M.D.**[1,2] **[Professor]**

[1]Department of Radiology, University of California, San Diego, 408 Dickinson St., San Diego, CA 92103-8226

[2]VA San Diego Healthcare System, 3350 La Jolla Village Drive MC-114, San Diego, CA 92161

1. Introduction: Short T2 Nature of Musculoskeletal Tissues

The tissues of the human body can be divided into those that are “visible” in the sense that they provide detectable signal with clinical MR systems and those that are “invisible” because their mean T2s or T2*s are too short to provide a detectable signal. All tissues have multicomponent T2s. This means that they contain a mixture of short and long T2 components. The invisible tissues have a majority of short T2 components and a minority of long T2 components. The latter components typically do not provide enough signal to be detectable in relation to image noise levels. Within these tissues (mean T2 < 10ms) it is possible to differentiate a first group including tendons, ligaments, and menisci with short mean T2s of about 1-10 ms, a second group including cortical bone and dentine with ultrashort mean T2s of 0.1-1 ms. There is also a third group including dental enamel, protons in membranes, and molecules as well as crystalline bone with super short mean T2s of less than 0.1 ms. From the standpoint of diagnosis and characterization of structural alteration in short and ultrashort T2 tissues, it would clearly be beneficial to obtain signal and manipulate contrast to achieve those goals. As knee injury, and the subsequent development of osteoarthrosis, as well as low back pain are encountered in the general population in epidemic proportions, we will focus on the characterization of short T2 tissues in the knee (cartilage and meniscus) and in the spine (intervertebral disc).

2. UTE MR Techniques and Utility In MSK Tissues

As noted above, many short T2 MSK tissues remain “invisible” or give very low signal intensity when imaged using conventional MRI. This is due to the inability of conventional pulse sequences to acquire data in the short T2 range. For example, a spin echo sequence has the minimum TE of ~10 ms, while a gradient echo sequence has a practical minimum TE of ~2 ms. MR signal from tissues with T2 value less than ~1 ms will have decayed away and will appear dark in conventional MR images.

Ultrashort TE (UTE) pulse sequences allow signal to be detected much earlier after excitation than with conventional sequences, and it is possible to detect short T2 relaxation components in tissues before they have decayed to low or zero levels (1-5). As a result, signal can be acquired from these tissues and can be visually assessed. In addition, the ability to acquire higher signals from tissues can be used to improve or make possible quantification of different tissue MR properties.

Corresponding Author: Christine B. Chung, Department of Radiology, University of California-San Diego, 408 Dickinson St., San Diego, CA 92103-8226, TEL: (858) 552-8585 ext 3589, FAX: (858) 296-7565, cbchung@ucsd.edu.

A number of UTE techniques focusing on the method of image acquisition (6-10) have been developed. These include are both two-dimensional (2D) and three-dimensional (3D) UTE sequences. A typical 2D UTE sequence employs half excitation pulses with radial mapping of k-space from the center out followed by another half excitation with the polarity of the slice selection gradient reversed (2,3,11) Data from the two half excitations are added to produce a single radial line of k-space. This process is repeated through 360 degrees. Raw data is typically mapped onto a 512×512 grid and reconstructed by 2D inverse Fourier Transformation (FT). 3D UTE sequences typically employs a short hard pulse excitation followed by 3D radial ramp sampling (9,10,12). Raw data is typically mapped onto a 3D Cartesian 256×256×256 grid and reconstructed by 3D inverse FT.

These 2D and 3D UTE sequences have been combined with techniques to modulate image contrast using suppression of long T2 water (9,13,14) and/or fat (12,15) signals using saturation or inversion nulling techniques. A dual adiabatic inversion recovery (DIR) preparation scheme (15) for example uses two long adiabatic inversion pulses are employed to invert and null long-T2 water and fat, respectively. Very short-T2 species (such as the calcified cartilage) are largely unaffected due to their fast transverse relaxation during the relatively slow adiabatic inversion process.

Quantitative techniques have been introduced to determine UTE T2*, UTE T1rho, and bi-component (i.e., long and short T2* components) of MSK tissues. T2* can be measured through exponential fitting of UTE images with a series of TE delays (16). T1rho can be measured through exponential fitting of UTE-T1rho images acquired at a series of spin-lock times (TSLs) (17). The UTE-T1rho sequence combines a regular spin-lock pulse cluster followed by regular UTE acquisition, and has been shown to be able to evaluate T1rho of both short and long T2 tissues (17). Regular UTE sequences can also be combined with variable TE acquisitions and bi-component analysis to quantify T2* and the fractions of short and long water components in MSK tissues (18).

3. MR Evaluation of the Knee: Articular Cartilage

3.1. Anatomy of Articular Cartilage

Articular cartilage (Figure 1, left) is a thin layer of connective tissue covering the ends of long bones. Articular cartilage functions as a load bearing, lubricating, and wear-resisting structure that facilitates joint motion. It is composed of sparsely distributed chondrocytes within a fluid-filled extracellular matrix that consists mainly of collagen and proteoglycans. The normal collagen network of cartilage is strong in tension (19), whereas the proteoglycans, due to a high density of negatively charged groups, swell in physiologic solutions and provide resistance to compression (20,21). Articular cartilage is anchored to subchondral bone via a ~100 μm thick (22), metabolically active (23) layer of calcified cartilage. This region of the osteochondral junction, including calcified cartilage and subchondral bone, is important for solute transport between the vasculature and articular cartilage (24).

Adult articular cartilage is inhomogeneous in structure and composition, varying mainly with depth from the articular surface (Figure 1). Collagen fibril orientation varies from being parallel to the articular surface to being perpendicular to it, from superficial layer to deep, respectively (25,26). Other properties of the collagen fibrils also vary with depth: the fibrils are generally fine and densely packed near the surface and thicker in the deep layers (27,28). In addition, the collagen network near the articular surface sometimes exhibits a preferred orientation that is generally in the same direction as the so-called splitline direction. These variations in collagen orientation influence magnetic resonance image appearance (29) and properties (30) when imaged in different orientations, due to the “magic angle effect.”

Proteoglycan content shows greater depth-variation, being about a third of the peak value near the surface and increasing to the peak high in the middle layer, as indicated by measurement of fixed charge density in human cartilage from the femoral condyle (31). Consistent with depth-varying structure and composition, MR properties such as T2 relaxation constant also varies with depth in articular cartilage (Figure 1, right).

Articular cartilage undergoes degeneration in osteoarthritis (OA), resulting in a number of structural, compositional and functional changes. Articular surface develops wear-lines and fissures with aging (32), which is a major contributor to biomechanical tensile weakening (33). Loss of proteoglycans is also associated with aging, which reduces compressive stiffness of the cartilage (34). Elevated levels of cytokines such as IL-1α in joints also degrade collagen and reduce mechanical strength (35). The role of deep and calcificied layer of cartilage in OA and cartilage degeneration has not been explored extensively. Calcified cartilage attaches overlying cartilage to subchondral bone, and has been implicated in the pathogenesis of cartilage degeneration (36). The calcified cartilage may thicken in osteoarthritis (37) and with overloading (38), while it thins near focal subchondral microcracks and lesions (39). Weakening of this layer, when subjected to injurious loading, may result in chondral delamination (40-42). Thus, non-invasive evaluation of calcified layer of cartilage is also of great interest along with evaluation of the overlying uncalcified cartilage

3.2. Conventional MRI of Articular Cartilage

Articular cartilage is often evaluated using radiologic methods (43). Plain radiography (44-46) of the anterior-posterior view are typically graded using decades-old Kellgren and Lawrence method (47), which lacks sensitivity to subtle changes in articular cartilage. Though computed tomography (CT) in conjunction with arthrography and ultrasonography offer higher spatial resolution, these methods also do not offer the soft tissue contrast provided by MR imaging, relegating their evaluation of cartilage to tissue loss with CT arthrography, and the superficial layer assessment with ultrasonography.

MR is generally regarded as one of the best available methods for evaluating injury and repair of the full-thickness, overlying uncalcified cartilage (48-50). It does so through exploiting MR properties intrinsic to all tissues, including T1 (spin-lattice relaxation time constant), T2 (spin-spin relaxation time constant) values, and T1rho (spin-lattice relaxation time constant in rotating frame) values. For example, for normal articular cartilage including the superficial and the middle layers, T1, T2, and T1rho values are in the order of ~1000 ms, ~40 ms, and ~60 ms, respectively (51). MR pulse sequences, by adjusting parameters of time-to-repeat (TR), time-to-echo (TE) and time-to-spin-lock (TSL), as well as a number of other parameters, are able to obtain images depicting many structures of the joint with preferred contrast. For example, proton density-weighted (PDw; long TR and short TE) and intermediate T2-weighted (T2w; long TR and intermediate TE) fast-suppressed spin echo or fast spin echo sequences highlight the synovial fluid (SF) while the cartilage has relatively low signal and contrast (52,53). T1-weighted (T1w; short TR and short TE) spin echo sequences give cartilage higher signal intensity than joint fluid (53), but is seldom used to assess intra-tissue signal variations. Example of PDw and T2w for a cadaveric patella is shown in Figure 2AB. These conventional clinical MR sequences have proven effective in the evaluation of cartilage lesions with surface irregularity and/or loss of thickness. These, along with fat saturated 3-D spoiled gradient echo imaging, have reported sensitivities of 93-94% for the detection of cartilage lesions (48,50,54).

Conventional quantitative MRI of articular cartilage is also beginning to be used in vivo, although it is not routinely used in clinical settings. In vitro studies have shown sensitivity of T2 (55), T1rho (56,57) and T1 (with delayed Gadolinium enhanced MRI of cartilage;

dGEMRIC) (58,59) to proteoglycan content of articular cartilage; higher T2 and T1rho values, and lower dGEMRIC index have been associated with loss of proteoglycans. In addition, biomechanical correspondence between T1rho (56,60) and dGEMRIC index (61) has been suggested, consistent with composition-function relation between proteoglycans and cartilage biomechanical properties (31,62). Examples of T2 and T1rho maps are shown in Figure 2CD, showing intra-tissue variations in quantitative MR properties that facilitate comparison against reference measures of function or composition. In vivo studies comparing the knee cartilage of volunteers and OA patients have found small but significant differences in T2 (63,64) T1rho (63) and dGEMRIC index (65). These quantitative techniques, especially T2 mapping, have been used often for evaluation of cartilage repair (66-70), where decreased T2 values and layer-stratification of T2 maps were generally associated with better repair. Quantitative MR methods have been applied to the hip cartilage as well (71-74).

3.3. UTE MRI of Articular Cartilage

Early application of UTE MRI to articular cartilage focused on direct visualization of deep layers. These included several in vivo studies which evaluated UTE MR appearance of knee articular cartilage without (1-3) or with (75) contrast agent. These studies described the presence of distinct linear signal intensity in the deepest layer of articular cartilage (Figure 2E). A recent validation study (76) compared UTE MRI and histology of experimental preparations, and determined that the presence of the deepest layer of uncalcified cartilage and the calcified cartilage, but not subchondral bone, results in this linear signal intensity in UTE MRI.

In order to modulate contrast of short T2 components, several techniques have been developed. These utilized suppression of long T2 water (9,13,14) and/or fat (12,15) signals using saturation or inversion nulling techniques. For example, a dual adiabatic inversion recovery (DIR) preparation technique two long adiabatic inversion pulses are employed to invert and null long-T2 water (such as that in the superficial layers of cartilage) and fat, respectively, to create a even higher image contrast for the calcified cartilage.

Figure 3 shows DIR UTE imaging of a normal patellar tissue sample. The imaging FOV of 8 cm, slice thickness of 0.7 mm and readout length of 512 result in an acquired voxel size of $0.16\times0.16\times0.7\ mm^3$, providing high resolution imaging of the patellar cartilage with a total scan time of 6 minutes. As has been previously noted, the high signal line represents a combination of signals from the deepest radial zone and the calcified cartilage. In comparison, the PD-FSE, T1-FSE and GE sequences do not allow identification of the calcified cartilage. The regular UTE sequence shows a high signal line, representing the deep radial cartilage and the calcified cartilage, however, there is limited contrast between the calcified cartilage and the superficial zones of articular cartilage. The DIR UTE sequence selectively suppresses signals from both fat and superficial zones of articular cartilage, providing a SNR of 15.6 ± 3.8 for the calcified cartilage, a CNR of 10.7 ± 3.2 between the calcified cartilage and superficial zones of articular cartilage, and 10.0 ± 2.5 between the calcified cartilage and fatty marrow. Compared to regular UTE imaging, DIR UTE increases the contrast between the calcified cartilage and superficial zones of cartilage by a factor of 5.8, and the contrast between the calcified cartilage and bone marrow fat by a factor of 4.2.

Figure 4 shows 3D DIR UTE imaging of a patella sample with a FOV of 6 cm, readout of 384, 20000 projections, providing a voxel size of $0.16\times0.16\times0.16\ mm^3$ under 100 minutes scan time. Regular 3D UTE without and with fat saturation were also performed for comparison. The 3D DIR UTE sequence provides high image contrast for the calcified cartilage with excellent suppression of the superficial layers of cartilage and fat. The high

isotropic spatial resolution minimizes partial volume artifacts associated with 2D DIR UTE imaging.

In addition to morphologic imaging, an increasing number of quantitative UTE MRI studies on articular cartilage are being performed. Basic approach here is similar to conventional T2* quantitative techniques; obtain multiple images at different echo time and perform a single- or multi-exponential fitting of the data. Using a single-component approach, the deepest layer of cartilage from six cadaveric femoral condyles was shown to have an average T2* of 1.3 msec (16), markedly lower than ~40 ms found in the majority of the overlying uncalcified cartilage, using conventional longer TE techniques (51).

Multiple T2* components in cartilage are also of great interest. Recently studies suggest the presence of both short and long T2 components in many tissues (77,78), including uncalcified, full-thickness articular cartilage (18,79,80). In one study of cartilage explants (81), both UTE (7) and long TE (multi-echo spin echo) techniques yielded opposing relation between the MR property and tissue degeneration, suggesting the short and long T2* components may change independently in degeneration. In another in vitro study (82) in which bovine nasal cartilage was degraded using trypsin to degrade collagen matrix and deplete proteoglycans, only the longer T2* values were increased with the treatment while the short T2 component did not change. In contrast, another study utilizing bi-component analysis (Figure 5) (18) on human patellar cartilage showed a marked increase in short T2* values with degeneration while no clear changes in long T2* values were observed. While it remains to be elucidated what mechanisms result in changes in short or long MR properties, and how to best determine these measures, continued research and development of short and ultrashort TE MRI has implication for novel early diagnosis of cartilage degeneration and patient care.

4. MR Evaluation of the Knee: Meniscus

4.1. Anatomy of Knee Meniscus

The meniscus of the knee is a predominantly fibrocartilaginous structure reinforced by highly ordered collagen fibers with a complex orientation. An understanding of this structure allows insight into basic biomechanics of the tissue, as it has been established that orientation of collagen fibrils reflects direction in which a tissue withstands tensile stress, thereby dictating mechanical stability (83). Approximately 98% of meniscal collagen is Type I, similar to that predominating in tendon and ligament. These collagen fibrils are able to withstand tension but have low compressive, flexural and torsional stiffness (83).

Fiber directions and types within the meniscus have been studied for many years, with more recent emphasis on results obtained using polarized light microscopy, scanning electron microscopy, confocal microscopy and immunohistochemistry (83-87). These techniques have shown at least 6 well-defined fiber groups that include: surface meshwork fibers, lamella layer, circumferential fibers, radial fibers, vertical (or superior-inferior (SI)) fibers, and meshwork fibers around the circumferential fibers.

The surface meshwork fibers comprise a layer that is approximately 30 nm thick that covers the meniscus. Beneath this layer lies the superficial lamella layer of types I and II collagen fibers extending to a depth of 150-200 μm. These fibers are variable in direction with a predominantly radial orientation at the periphery, and a circumferential orientation more centrally with variations from this pattern between the tibial and femoral surfaces as well as within the anterior and posterior horns of the menisci. The majority of the meniscus is composed of predominantly circumferential bundles of type I collagen fibers with a continuation of many of these fibers into the root ligaments of the menisci. Radial fibers

may be condensed to form larger collagen bundles (radial ties) and may also appear as sheets. They mainly consist of type I collagen with areas of type II collagen within them. They typically extend from the outer margin of the meniscus centrally in a generally horizontal direction to end within the meniscus itself, or at the femoral or tibial surface of the meniscus (Figure 6). The patterns may vary between the anterior horn with shorter earlier branching fibers, and the posterior horn with thicker and longer fibers or sheets. Vertical or SI fibers are seen beneath the lamella layer centrally, deep to the outer margin of the meniscus and at other locations. They may, at least in part, represent arborization of radial fibers. The meshwork fibers surrounding the circumferential fibers contain collagen types I and II fibers in the white zone, and type I fibers only in the red zone.

The distribution of the meniscal fibrillar pattern varies from its inner margin to its periphery. The inner region of the meniscus contains predominantly circumferentially oriented fibers in the lamellar layer, some deeper circumferential fibers, and an attenuated fiber meshwork around the circumferential fibers. There is debate about the extent of radial fibers in this region. In addition, the more central region of the meniscus is more cartilaginous, while the more peripheral region is more fibrous (Figure 7) (88). The more peripheral adult meniscus (the red or vascular zone) has a blood supply in areas adjacent to perimeniscal tissue while the more central region (the white zone) is avascular (Figure 8) (89). At its peripheral margin, loose connective tissue and fat continuous with perimeniscal tissue enters the meniscal substance.

4.2. Conventional MRI of Knee Meniscus

Initial clinical magnetic resonance (MR) studies of the meniscus were performed using solenoidal magnets with the plane of the meniscus perpendicular to the static magnetic field (B_0) and typically employed T1 weighted, mobile proton density (ρ_m) weighted and/or T2 weighted conventional spin echo (SE) sequences with echo times (TEs) of about 10-40 ms (90-92). With these sequences, and the meniscus perpendicular to B_0, the normal meniscus displayed little or no signal. It has a relatively short mean T2 and with conventional clinical SE TEs, the MR signal from most, if not all of the meniscus decays to a low or zero level before the MR signal can be detected and spatially encoded. This low signal level provided a useful dark background against which higher signal abnormalities in the meniscus could be recognized and validated surgically and/or histologically (93-96). Utilizing conventional 2D MR sequences, accuracy in diagnosing meniscal tears ranges from 70-90% compared with surgery (97,98). With more recently developed 3D sequences, no significant increase in the accuracy of meniscal tear detection could be demonstrated (99). However, using conventional MR techniques for detection of pathology results in late-stage diagnosis (100,101). Early diagnosis of injury can be performed with quantitative techniques that evaluate the composition of both cartilage and menisci, including collagen fibers, proteoglycan, and water (102,103). Specifically, intrinsic MR properties of tissues include T2, which is related to structural changes (collagen orientation) (5,104) and T1rho, which is inversely related to biochemical changes (proteoglycan content) (105). Preliminary data suggests that quantitative T1rho of cartilage can be useful in detecting changes in patients with osteoarthrosis (106), as previously noted. More recently, both of these quantitative MR measurements have been shown to detect and quantify severity of meniscal degeneration and are correlated with worse clinical symptoms (64).

Particularly challenging in the evaluation of the knee on conventional clinical MR sequences, has been the identification of meniscal calcification and potential imaging pitfalls therein. Calcification, as meniscal tissue, has a relatively short intrinsic T2 relaxation time creating suboptimal or aberrant contrast between the two that can result in ability to detect signal, or misinterpretation of signal as meniscal tear (107,108). In addition, the lack of

spatial resolution with standard clinical sequences provides an additional challenge for the visualization of small, punctate calcifications (Figure 11).

4.3. UTE MRI of Knee Meniscus

UTE MRI affords a greater flexibility in morphologic evaluation of knee meniscus. We have used 2D and 3D UTE techniques to study cadaveric meniscus at a high resolution. Using a 2D technique, effect of varying TEs from 0.012 ms to 12 ms illustrates (Figure 9) the advantages of optimizing signal from the short T2 tissue of meniscus, as well as allowing for contrast optimization. The meniscus consists of fibrillar structures as previously noted, with short T2 values ~10 ms, as well as interfibrillar fibrocartilage, with much shorter T2 value, that decays rapidly by TE~10 ms. Using the shortest TE less, with values less than 1 ms, the entire meniscus can be seen with high signal intensity. Using short TE values of 3~6 ms, structures are visible with arguably better contrast. At higher TE values on the order of 12 ms (short TE by clinical standard), regions of fibrocartilage exhibited very low signal, and would unlikely depict subtle changes in regional T2 properties. A 3D UTE MRI technique was developed and implemented by our group to evaluate meniscal tissue. Imaging parameters were FOV=5 cm, TR=500 ms, TE=0.008, 7, and 14 ms, Matrix=384^3. High resolution isotropic voxels afford a detailed morphologic evaluation of meniscal tissue in any arbitrary planes; Figure 10 shows a cadaveric sample in anatomic imaging planes. Interfibrillar fibrocartilage has a high signal at ultrashort TE, while the fibrillar network is more prominent at longer TEs.

In addition to normal morphology, 3D UTE MRI techniques enable direct visualization and quantification of meniscal calcification, seen in radiographs. Subtraction of the 2^{nd} echo image from the first image selectively showed meniscal calcification with high signal and contrast, as shown in Figure 11. There was residual signal from fat and meniscal fibers oriented parallel to the B_0 field. This signal showed significant decay between the first FID and the second image, resulting in a relatively high signal on the subtraction image.

Quantitative UTE MR evaluation of menisci have also been performed (17). UTE-T1rho (tailored for short T2) and MAPSS T1rho (tailored for long T2) (109) sequences have been compared for *in vivo* imaging of the menisci as well as the femoral-tibia cartilage. The UTE T1rho sequence was first applied to image the meniscus in a healthy, asymptomatic volunteer. The acquisition parameters were: FOV = 16 cm, TR = 400 ms, TSL =0.2/1/5/25/40 ms, TE=0.008 ms, BW=±62.5 kHz, readout = 512, slice thickness = 3 mm, 301 half projections, NEX = 2, scan duration=4 minutes for each TSL. The MAPPS T1rho sequence had a much longer minimal TE of 2.4 ms but showed otherwise similar results. Figure 12 shows the corresponding images and the T1rho fitting for the meniscus. Clearly, UTE T1ρ provides much higher signal for meniscus, and shorter T1rho values (~9 ms). The MAPPS sequence provides signal from the longer T2 component of meniscus, resulting in higher T1rho values (~13 ms).

4. MR Evaluation of the Spine: Intervertebral Disc

4.1. Anatomy of Intervertebral Disc

The human spine comprises 23 intervertebral discs (IVD) positioned between vertebrae that facilitate back movement. The IVDs are bounded peripherally by the anterior and posterior longitudinal ligaments of the spine and axially by the superior and inferior cartilaginous endplates (110). IVDs have a heterogeneous structure, with a central nucleus pulposus (NP) surrounded by peripheral anulus fibrosus (AF). In adults, healthy nucleus pulposi are well-hydrated and rich in glycosaminoglycans which resist compression, while the anulus fibrosi have markedly less water content, consisting of concentric bundles of fibrous lamellae bundles surrounded by extracellular matrices.

The structure and composition of the IVD in adults varies with location within the disc. The AF of an adult lumbar disc consists of over twenty lamellar sheets of parallel collagen fibers. The lamellae within a disc alternate in orientation, ~±25° relative to the endplates (111,112). Such structure allows for resisting large tensile forces in the AF induce during spine movement, including bending, rotation, axial compression. The lamellar structure of the AF is disrupted in disc herniation (113) but is not routinely visualized with clinical MR imaging. Inner or central portions of AF, close to NP, contain more proteoglycans between layers of collagen fibrils (114), when compared to the outer AF. In the central region of the disc, NP contains less collagen and the collagen fibrils have random orientation. There is an abundant amount of proteoglycans in the interfibrillar matrix of NP. Since proteoglycans attract water while the collagen network resists swelling, water content is the lowest in the outer AF and the highest in the NP. Cellularity is also different between NP and AF; in the adult NP, the cell density is ~4 million cells/ml while in AF, it is ~9 million cells/ml (115). This makes IVD one of the most sparsely cellular tissues in the body (116).

Cartilaginous endplates (CEP), also known as vertebral endplates (110), form an interface between the disc proper and vertebral body. The normal CEP in mature adults consists of layers of uncalcified and calcified cartilage (117), and is ~ 1 mm thick (118). CEP is slightly thinner in the central region compared with the periphery (118,119). Collagen fibers of the inner lamellae of the AF enter the CEP at an angle and swing centrally to become parallel with the CEP (110). The vertebral body provides a bed of capillaries that adhere directly onto the CEP, penetrating the calcified layer and abutting directly onto the uncalcified cartilage (120). Due to the avascular nature of the IVD in adults, the homeostasis of the disc cells and matrices is dependent on the diffusion of metabolites into and out of the disc (121-123). A number of studies over the years have focused on the evaluation of the endplate region of the disc, and the relationship between changes in this region and disc degeneration (122,124-126).

Spine-related pain is a major cause of disability in the United States and involves a large proportion of the population (127). The pain can be caused by degeneration or injury in various components of the lumbar spine, including and frequently the IVD (127), paravertebral muscles and zygapophyseal joints. Specifically, IVD degeneration is believed to be a source of chronic pain (128) and associated conditions such as disc herniation are a known cause of radicular pain (129). Internal disc disruption, focal and distinct change in annular morphology of the disc, has also been correlated strongly with pain on disc stimulation (130,131). On the other hand, it is clinically recognized that disc degeneration is also observed in patients without low back pain (132,133). The relationship between IVD degeneration and pain is complex.

While the exact pathogenesis is unknown, age-dependent degenerative disc disease may be related to changes in the CEP. With increasing age after maturity and in certain diseases such as scoliosis, there are structural and compositional changes in the CEP that may contribute to disc degeneration. Gradual thinning of the CEP along with occlusion of vascular canals by ectopic calcification has been suggested (134), which has been hypothesized to be due to progressive resorption and advance of the subchondral bone plate. Similarly, in scoliosis, calcification occurs, ranging from isolated deposits of calcium salts to ossification throughout the thickness of the CEP (125). In an in vitro study of the CEP of cadaveric samples, complete occlusion of vascular canals in histology occurred more frequently in samples from aged donors (which tended to have more degenerate discs as well) (135). Aging is also associated with an increase in immunostaining for type × collagen (136), a calcium-binding collagen, in the region of the CEP, suggesting increased propensity of the CEP to undergo calcification with aging, and possible etiology for subsequent disc degeneration (137). A non-invasive and sensitive method to detect such changes in the CEP

would be of considerable value for early diagnosis, and improve understanding of the pathogenesis of disc degeneration.

4.2. Conventional MRI of Intervertebral Disc

With the advent of non-invasive MRI, it has become possible to observe morphologic and signal changes in intervertebral discs, specifically the NP, with high sensitivity and specificity. In contrast to plain radiography and computed tomography, MRI allows direct evaluation of the NP without interference from bony changes. MRI has been used to detect disc herniation and nerve root compression based on morphology, with a high degree of accuracy (138,139). For evaluation of the internal structure of discs, morphologic grading systems have been devised including intradiscal signal intensity and morphology, usually based on T2-weighted spin echo or fast spin echo images in the sagittal plane (140,141). These have been used in a number of studies to determine biological-treatment efficacy on the MR appearance of discs (142,143) and to classify patients into groups based on MRI (144,145).

With advances in quantitative MRI techniques, numerous studies have shown a correlation between the biochemical content of the disc and its MR properties. During the early phase of disc degeneration, loss of proteoglycans and collagen type II occurs (146). These changes are associated with decreased water content (147) and changes in MR properties (148). Both T1 (spin-lattice relaxation time) and T2 (spin-spin relaxation time) of the disc correlate strongly with water content (149,150), both values increasing when water content increases. This is also consistent with diurnal changes in the T2 of discs (151,152). A correlation between T2 values and proteoglycan content has also been found (147,153). More recently, T1rho (spin-lattice relaxation in rotating frame) which in theory is sensitive to slow movement (relative to water) of macro-molecules such as proteoglycans has been studied (105). Examples of a young normal (27 years old male) and a middle-aged degenerate (57 years old male) cadaveric lumbar spines, and their T2 and T1rho maps obtained at 3T, are shown in Figure 13. Spine segments, ~10 inches in length, were imaged using two sequences: a 2D spiral chopped magnetization preparation sequence (154) (time-to-spin lock, or TSL, of 0, 10, 40 and 80 ms) was used to quantify T1rho values of the disc (Figure 13AB; axial plane, field of view=12 cm, slice thickness=3 mm) and a multi-echo (time-to-echo, or TE, of 10 to 80 ms in 8 increments) spin-echo sequence was used to quantify T2 values (Figure 13CD; sagittal plane, field of view=20 cm, slice thickness=3 mm), on a per-voxel basis. Normal discs had high T1rho (Figure 13A) and T2 (Figure 13C) values and pristine-white and gelatinous NP grossly (Figure 13E), in contrast to degenerate discs with low MR values (Figure 13BD) and desiccated gross morphology (Figure 13F). Collapse in disc height was also evident in sagittal MRI of the disc with the lowest T1rho values (Figure 13B). There are additional pulse sequences, including diffusion-weighted imaging (150,152,155), that are sensitive to self-diffusivity of water within the disc, and MR spectroscopy (156,157) which can be used to monitor concentrations of certain tissue metabolites including lactate which may be relevant to discogenic pain (158).

4.2. UTE and Short TE MRI of Intervertebral Disc

Despite the availability of a variety of MR imaging sequences for evaluation of intervertebral discs, certain regions of AF and the CEP has not been evaluated extensively using conventional MRI techniques. This is mainly due to low signal intensity of these tissues exhibits in images obtained using conventional MR sequences, due to short T2 values (~1 ms or less) that are orders of magnitude less than those of the NP of the disc (~100 ms, Figure 13C).

The gradient echo techniques have the ability to measure T2 values in the 1 to 2 ms range, though they do so at the expense of spatial resolution, increased slice thickness and bandwidth. Short TE gradient echo techniques may be useful for MR imaging of the AF, with a consideration for the magic angle effects (29,30,159). Many fibrous structures in body, including the AF, exhibit signal intensity and T2 values that are dependent of its orientation relative to the main magnetic field (29). A recently introduced technique (160), utilizing a 3D spoiled gradient echo sequence along with multiple sample-orientations, was applied to human IVD to reveal detailed AF structure (161). A human lumbar bone-disc-bone segment was imaged at 3T at six different orientations: TR=38 ms, TE=6.4 ms, FA=20°, FOV=6 cm, axial slice=0.2 mm, matrix=384×384. Images were spatially-registered and the minimum and the coefficient of variation was determined on per-voxel basis. On the axial minimum intensity projection images, low signal lamellae (Figure 14A, arrows) were demonstrated throughout the disc, being the thickest near the periphery and thinner centrally. On a mid-sagittal image, an inverted radial bulge of the lamellae (Figure 13B, arrows) was identified, possibly due to dehydration of the NP and a partial collapse of the disc. A thin fibrous layer was observed between the nucleus pulposus and the cartilaginous end plate. The lamellar regions of the AF had high coefficients of variation (Figure 13C, arrows), suggesting that the region had greater changes in signal intensity as the orientation of the sample was varied, as expected for fiber structures experiencing the magic angle effect. Regions of the extracellular matrix and nucleus showed little variation.

The ultrashort time-to-echo (UTE) technique have been used recently to image spine tissues with even shorter T2 than the AF (4,5,162,163). Many previously “MR-invisible” tissues of the spine including longitudinal ligaments (Figure 15BD, curved arrows), ligamentum flavum, and the CEP (164) have been imaged directly. The CEP of the disc normally appears as dark linear region in MR images from conventional MRI sequences such as T2-weight spin echo (Figure 15AC). Using UTE MR technique, the CEP region is now visible (Figure 15BD). In the majority of spine segments with normal disc and vertebral bodies, this UTE MR signal from the CEP region characteristically appears as a high intensity line (Figure 15BD, arrows), consistent with the known CEP anatomy (110). In a minority of spines, while the conventional MRI shows normal disc and the subchondral bone (Figure 15C), there can be abnormal changes seen in the UTE MR signal in the CEP region, such as thinning or loss of the characteristic signal intensity focally (Figure 15D, triangle). Preliminary studies suggest that abnormality of the CEP in UTE MRI is significantly associated with disc degeneration (163), as well as increased endplate roughness, suggesting calcification (162). Direct evaluation of the CEP using UTE MRI, along with functional evaluation of the CEP using methods such as time-resolved contrast-enhanced MRI (145), will be useful for better understanding of nutritional health of the IVD, as well as stratification of patients that could respond well to biological treatments (165).

Acknowledgments

NIH, VA merit, General Electric

References

1. Gold GE, Thedens DR, Pauly JM, et al. MR imaging of articular cartilage of the knee: new methods using ultrashort TEs. AJR Am J Roentgenol. 1998; 170:1223–1226. [PubMed: 9574589]
2. Gatehouse PD, Thomas RW, Robson MD, et al. Magnetic resonance imaging of the knee with ultrashort TE pulse sequences. Magnetic Resonance Imaging. 2004; 22:1061–1067. [PubMed: 15527992]
3. Young IR, Bydder GM. Magnetic resonance: new approaches to imaging of the musculoskeletal system. Physiol Meas. 2003; 24:R1–23. [PubMed: 14658774]

4. Robson MD, Gatehouse PD, Bydder M, et al. Magnetic resonance: an introduction to ultrashort TE (UTE) imaging. J Comput Assist Tomogr. 2003; 27:825–846. [PubMed: 14600447]
5. Gatehouse PD, Bydder GM. Magnetic resonance imaging of short T2 components in tissue. Clin Radiol. 2003; 58:1–19. [PubMed: 12565203]
6. Du J, Bydder M, Takahashi AM, et al. Two-dimensional ultrashort echo time imaging using a spiral trajectory. Magnetic Resonance Imaging. 2008; 26:304–312. [PubMed: 18096346]
7. Qian Y, Boada FE. Acquisition-weighted stack of spirals for fast high-resolution three-dimensional ultra-short echo time MR imaging. Magn Reson Med. 2008; 60:135–145. [PubMed: 18581326]
8. Idiyatullin D, Corum C, Park JY, et al. Fast and quiet MRI using a swept radio frequency. J Magn Reson. 2006; 181:342–349. [PubMed: 16782371]
9. Du J, Bydder M, Takahashi AM, et al. Short T2 contrast with three-dimensional ultrashort echo time imaging. Magnetic Resonance Imaging. 2011; 29:470–482. [PubMed: 21440400]
10. Rahmer J, Börnert P, Groen J, et al. Three-dimensional radial ultrashort echo-time imaging with T2 adapted sampling. Magnetic resonance in medicine : official journal of the Society of Magnetic Resonance in Medicine / Society of Magnetic Resonance in Medicine. 2006; 55:1075–1082. [PubMed: 16538604]
11. Lu, A.; Daniel, BL.; Pauly, KB. Proceedings of the 14th Annual Meeting of ISMRM. 2006. Improved slice excitation for ultrashort TE imaging with B_0 and linear eddy current correction; p. 2381
12. Wu Y, Ackerman JL, Chesler DA, et al. Density of organic matrix of native mineralized bone measured by water- and fat-suppressed proton projection MRI. Magnetic resonance in medicine : official journal of the Society of Magnetic Resonance in Medicine / Society of Magnetic Resonance in Medicine. 2003; 50:59–68. [PubMed: 12815679]
13. Techawiboonwong A, Song HK, Wehrli FW. In vivo MRI of submillisecond T(2) species with two-dimensional and three-dimensional radial sequences and applications to the measurement of cortical bone water. NMR in biomedicine. 2008; 21:59–70. [PubMed: 17506113]
14. Sussman MS, Pauly JM, Wright GA. Design of practical T2-selective RF excitation (TELEX) pulses. Magnetic resonance in medicine : official journal of the Society of Magnetic Resonance in Medicine / Society of Magnetic Resonance in Medicine. 1998; 40:890–899. [PubMed: 9840834]
15. Du J, Takahashi AM, Bae WC, et al. Dual inversion recovery, ultrashort echo time (DIR UTE) imaging: creating high contrast for short-T(2) species. Magnetic resonance in medicine : official journal of the Society of Magnetic Resonance in Medicine / Society of Magnetic Resonance in Medicine. 2010; 63:447–455. [PubMed: 20099332]
16. Du J, Takahashi AM, Chung CB. Ultrashort TE spectroscopic imaging (UTESI): application to the imaging of short T2 relaxation tissues in the musculoskeletal system. Journal of magnetic resonance imaging : JMRI. 2009; 29:412–421. [PubMed: 19161197]
17. Du J, Carl M, Diaz E, et al. Ultrashort TE T1rho (UTE T1rho) imaging of the Achilles tendon and meniscus. Magn Reson Med. 2010; 64:834–842. [PubMed: 20535810]
18. Du J, Pauli C, Diaz E, et al. Free and bound water evaluation of articular cartilage. Proc Int'l Soc Magn Reson Med. 2011; 19:565.
19. Mow, VC.; Zhu, W.; Ratcliffe, A. Structure and function of articular cartilage and meniscus. In: Mow, VC.; Hayes, WC., editors. Basic Orthopaedic Biomechanics. New York: Raven Press; 1991. p. 143-198.
20. Maroudas, A. Physico-chemical properties of articular cartilage. In: Freeman, MAR., editor. Adult Articular Cartilage. 2nd. Tunbridge Wells, England: Pitman Medical; 1979. p. 215-290.
21. Buschmann MD, Grodzinsky AJ. A molecular model of proteoglycan-associated electrostatic forces in cartilage mechanics. J Biomech Eng. 1995; 117:179–192. [PubMed: 7666655]
22. Lane LB, Bullough PG. Age-related changes in the thickness of the calcified zone and the number of tidemarks in adult human articular cartilage. J Bone Joint Surg Br. 1980; 62:372–375. [PubMed: 7410471]
23. Green WT Jr, Martin GN, Eanes ED, et al. Microradiographic study of the calcified layer of articular cartilage. Arch Pathol. 1970; 90:151–158. [PubMed: 5433599]
24. Lyons TJ, Stoddart RW, McClure SF, et al. The tidemark of the chondro-osseous junction of the normal human knee joint. J Mol Histol. 2005; 36:207–215. [PubMed: 15900412]

25. Aspden RM, Hukins DWL. Collagen organization in articular cartilage, determined by x-ray diffraction, and its relationship to tissue function. Proc R Soc Lond B. 1981; 212:299–304. [PubMed: 6115394]
26. Broom, ND. The collagen framework of articular cartilage: Its profound influence on normal and abnormal load-bearing function. In: Nimni, ME., editor. Collagen: Chemistry, Biology, and Biotechnology. Vol. II. Boca Raton, FL: CRC Press, Inc.; 1988. p. 243-265.
27. Lane JM, Weiss C. Review of articular cartilage collagen research. Arthritis Rheum. 1975; 18:553–562. [PubMed: 173345]
28. Muir H, Bullough P, Maroudas A. The distribution of collagen in human articular cartilage with some of its physiological implications. J Bone Joint Surg Br. 1970; 52:554–563. [PubMed: 4247851]
29. Erickson SJ, Prost RW, Timins ME. The “magic angle” effect: background physics and clinical relevance. Radiology. 1993; 188:23–25. [PubMed: 7685531]
30. Du J, Pak BC, Znamirowski R, et al. Magic angle effect in magnetic resonance imaging of the Achilles tendon and enthesis. Magnetic Resonance Imaging. 2009; 27:557–564. [PubMed: 19022600]
31. Chen SS, Falcovitz YH, Schneiderman R, et al. Depth-dependent compressive properties of normal aged human femoral head articular cartilage: relationship to fixed charge density. Osteoarthritis Cartilage. 2001; 9:561–569. [PubMed: 11520170]
32. Kempson GE. Age-related changes in the tensile properties of human articular cartilage: a comparative study between the femoral head of the hip joint and the talus of the ankle joint. Biochim Biophys Acta. 1991; 1075:223–230. [PubMed: 1954224]
33. Bae WC, Wong VW, Hwang J, et al. Wear-lines and split-lines of human patellar cartilage: relation to tensile biomechanical properties. Osteoarthritis Cartilage. 2008; 16:841–845. [PubMed: 18248747]
34. Kempson GE. Mechanical properties of articular cartilage and their relationship to matrix degradation and age. Ann Rheum Dis. 1975; 34(2):111–114.
35. Temple MM, Xue Y, Chen MQ, et al. Interleukin-1a induction of tensile weakening associated with collagen degradation in bovine articular cartilage. Arthritis Rheum. 2006; 54:3267–3276. [PubMed: 17009261]
36. Boyde A, Riggs CM, Bushby AJ, et al. Cartilage damage involving extrusion of mineralisable matrix from the articular calcified cartilage and subchondral bone. Eur Cell Mater. 2011; 21:470–478. [PubMed: 21623571]
37. Hwang J, Bae WC, Shieu W, et al. Increased hydraulic conductance of human articular cartilage and subchondral bone plate with progression of osteoarthritis. Arthritis Rheum. 2008; 58:3831–3842. [PubMed: 19035476]
38. Burr DB. Anatomy and physiology of the mineralized tissues: role in the pathogenesis of osteoarthrosis. Osteoarthritis Cartilage. 2004; 12(A):S20–30. [PubMed: 14698637]
39. Boyde A, Firth EC. High resolution microscopic survey of third metacarpal articular calcified cartilage and subchondral bone in the juvenile horse: possible implications in chondro-osseous disease. Microsc Res Tech. 2008; 71:477–488. [PubMed: 18320577]
40. Chiang ER, Ma HL, Chen TH. Chondral delamination injury over tibial plateau mimicking a torn lateral discoid meniscus. Clin J Sport Med. 2010; 20:120–121. [PubMed: 20215895]
41. Kendell SD, Helms CA, Rampton JW, et al. MRI appearance of chondral delamination injuries of the knee. AJR Am J Roentgenol. 2005; 184:1486–1489. [PubMed: 15855101]
42. Levy AS, Lohnes J, Sculley S, et al. Chondral delamination of the knee in soccer players. Am J Sports Med. 1996; 24:634–639. [PubMed: 8883684]
43. Altman RD. Criteria for classification of clinical osteoarthritis. J Rheumatol Suppl. 1991; 27:10–12. [PubMed: 2027107]
44. Reginster JY, Deroisy R, Rovati LC, et al. Long-term effects of glucosamine sulphate on osteoarthritis progression: a randomised, placebo-controlled clinical trial. Lancet. 2001; 357:251–256. [PubMed: 11214126]

45. Pavelka K, Gatterova J, Olejarova M, et al. Glucosamine sulfate use and delay of progression of knee osteoarthritis: a 3-year, randomized, placebo-controlled, double-blind study. Arch Intern Med. 2002; 162:2113–2123. [PubMed: 12374520]
46. Brandt KD, Mazzuca SA, Katz BP, et al. Effects of doxycycline on progression of osteoarthritis: results of a randomized, placebo-controlled, double-blind trial. Arthritis Rheum. 2005; 52:2015–2025. [PubMed: 15986343]
47. Kellgren JH, Lawrence JS. Radiological assessment of osteo-arthrosis. Ann Rheum Dis. 1957; 16:494–502. [PubMed: 13498604]
48. Disler DG, McCauley TR, Wirth CR, et al. Detection of knee hyaline cartilage defects using fat-suppressed three-dimensional spoiled gradient-echo MR imaging: comparison with standard MR imaging and correlation with arthroscopy. AJR Am J Roentgenol. 1995; 165:377–382. [PubMed: 7618561]
49. Hodler J, Resnick D. Current status of imaging of articular cartilage. Skeletal Radiol. 1996; 25:703–709. [PubMed: 8958614]
50. Recht MP, Piraino DW, Paletta GA, et al. Accuracy of fat-suppressed three-dimensional spoiled gradient-echo FLASH MR imaging in the detection of patellofemoral articular cartilage abnormalities. Radiology. 1996; 198:209–212. [PubMed: 8539380]
51. Taylor C, Carballido-Gamio J, Majumdar S, et al. Comparison of quantitative imaging of cartilage for osteoarthritis: T2, T1rho, dGEMRIC and contrast-enhanced computed tomography. Magnetic Resonance Imaging. 2009; 27:779–784. [PubMed: 19269769]
52. Alparslan L, Minas T, Winalski CS. Magnetic resonance imaging of autologous chondrocyte implantation. Semin Ultrasound CT MR. 2001; 22:341–351. [PubMed: 11513158]
53. Potter HG, Foo LF. Magnetic resonance imaging of articular cartilage: trauma, degeneration, and repair. Am J Sports Med. 2006; 34:661–677. [PubMed: 16365371]
54. Bredella MA, Tirman PF, Peterfy CG, et al. Accuracy of T2-weighted fast spin-echo MR imaging with fat saturation in detecting cartilage defects in the knee: comparison with arthroscopy in 130 patients. AJR Am J Roentgenol. 1999; 172:1073–1080. [PubMed: 10587150]
55. Li X, Cheng J, Lin K, et al. Quantitative MRI using T1ρ and T2 in human osteoarthritic cartilage specimens: correlation with biochemical measurements and histology. Magnetic Resonance Imaging. 2011; 29:324–334. [PubMed: 21130590]
56. Wheaton AJ, Dodge GR, Elliott DM, et al. Quantification of cartilage biomechanical and biochemical properties via T1rho magnetic resonance imaging. Magn Reson Med. 2005; 54:1087–1093. [PubMed: 16200568]
57. Duvvuri U, Kudchodkar S, Reddy R, et al. T(1rho) relaxation can assess longitudinal proteoglycan loss from articular cartilage in vitro. Osteoarthritis Cartilage. 2002; 10:838–844. [PubMed: 12435327]
58. Gillis A, Bashir A, McKeon B, et al. Magnetic resonance imaging of relative glycosaminoglycan distribution in patients with autologous chondrocyte transplants. Invest Radiol. 2001; 36:743–748. [PubMed: 11753146]
59. Gray ML, Burstein D, Xia Y. Biochemical (and functional) imaging of articular cartilage. Semin Musculoskelet Radiol. 2001; 5:329–343. [PubMed: 11745049]
60. Bae WC, Statum S, Biswas R, et al. Sensitivity of Quantitative UTE MRI to Degradation of Human TMJ Discs. Proc Int'l Soc Magn Reson Med. 2011; 19:569.
61. Samosky JT, Burstein D, Eric Grimson W, et al. Spatially-localized correlation of dGEMRIC-measured GAG distribution and mechanical stiffness in the human tibial plateau. J Orthop Res. 2005; 23:93–101. [PubMed: 15607880]
62. Maroudas A. Balance between swelling pressure and collagen tension in normal and degenerate cartilage. Nature. 1976; 260:808–809. [PubMed: 1264261]
63. Li X, Benjamin Ma C, Link TM, et al. In vivo T(1rho) and T(2) mapping of articular cartilage in osteoarthritis of the knee using 3 T MRI. Osteoarthr Cartil. 2007; 15:789–797. [PubMed: 17307365]
64. Zarins ZA, Bolbos RI, Pialat JB, et al. Cartilage and meniscus assessment using T1rho and T2 measurements in healthy subjects and patients with osteoarthritis. Osteoarthritis Cartilage. 2010; 18:1408–1416. [PubMed: 20696262]

65. Williams A, Sharma L, McKenzie CA, et al. Delayed gadolinium-enhanced magnetic resonance imaging of cartilage in knee osteoarthritis: findings at different radiographic stages of disease and relationship to malalignment. Arthritis Rheum. 2005; 52:3528–3535. [PubMed: 16255024]
66. Oneto JMM, Ellermann J, LaPrade RF. Longitudinal evaluation of cartilage repair tissue after microfracture using T2-mapping: a case report with arthroscopic and MRI correlation. Knee Surg Sports Traumatol Arthrosc. 2010; 18:1545–1550. [PubMed: 20505925]
67. Domayer SE, Welsch GH, Nehrer S, et al. T2 mapping and dGEMRIC after autologous chondrocyte implantation with a fibrin-based scaffold in the knee: preliminary results. Eur J Radiol. 2010; 73:636–642. [PubMed: 19157740]
68. Welsch GH, Mamisch TC, Domayer SE, et al. Cartilage T2 assessment at 3-T MR imaging: in vivo differentiation of normal hyaline cartilage from reparative tissue after two cartilage repair procedures--initial experience. Radiology. 2008; 247:154–161. [PubMed: 18372466]
69. Mamisch TC, Trattnig S, Quirbach S, et al. Quantitative T2 mapping of knee cartilage: differentiation of healthy control cartilage and cartilage repair tissue in the knee with unloading--initial results. Radiology. 2010; 254:818–826. [PubMed: 20123898]
70. Kim M, Foo LF, Uggen C, et al. Evaluation of early osteochondral defect repair in a rabbit model utilizing fourier transform-infrared imaging spectroscopy, magnetic resonance imaging, and quantitative T2 mapping. Tissue engineering Part C, Methods. 2010; 16:355–364. [PubMed: 19586313]
71. Miese FR, Zilkens C, Holstein A, et al. Assessment of early cartilage degeneration after slipped capital femoral epiphysis using T2 and T2* mapping. Acta Radiol. 2011; 52:106–110. [PubMed: 20954816]
72. Kim YJ, Jaramillo D, Millis MB, et al. Assessment of early osteoarthritis in hip dysplasia with delayed gadolinium-enhanced magnetic resonance imaging of cartilage. J Bone Joint Surg Am. 2003; 85-A:1987–1992. [PubMed: 14563809]
73. Mamisch TC, Kain MSH, Bittersohl B, et al. Delayed gadolinium-enhanced magnetic resonance imaging of cartilage (dGEMRIC) in Femoacetabular impingement. J Orthop Res. 2011
74. Sur S, Mamisch TC, Hughes T, et al. High resolution fast T1 mapping technique for dGEMRIC. Journal of magnetic resonance imaging : JMRI. 2009; 30:896–900. [PubMed: 19787737]
75. Gatehouse PD, He T, Puri BK, et al. Contrast-enhanced MRI of the menisci of the knee using ultrashort echo time (UTE) pulse sequences: imaging of the red and white zones. The British journal of radiology. 2004; 77:641–647. [PubMed: 15326040]
76. Bae WC, Dwek JR, Znamirowski R, et al. Ultrashort echo time MR imaging of osteochondral junction of the knee at 3 T: identification of anatomic structures contributing to signal intensity. Radiology. 2010; 254:837–845. [PubMed: 20177096]
77. Nyman JS, Ni Q, Nicolella DP, et al. Measurements of mobile and bound water by nuclear magnetic resonance correlate with mechanical properties of bone. Bone. 2008; 42:193–199. [PubMed: 17964874]
78. Horch RA, Nyman JS, Gochberg DF, et al. Characterization of 1H NMR signal in human cortical bone for magnetic resonance imaging. Magn Reson Med. 2010; 64:680–687. [PubMed: 20806375]
79. Reiter DA, Lin PC, Fishbein KW, et al. Multicomponent T2 relaxation analysis in cartilage. Magn Reson Med. 2009; 61:803–809. [PubMed: 19189393]
80. Qian Y, Williams AA, Chu CR, et al. Multicomponent T2* mapping of knee cartilage: technical feasibility ex vivo. Magn Reson Med. 2010; 64:1426–1431. [PubMed: 20865752]
81. Williams A, Qian Y, Bear D, et al. Assessing degeneration of human articular cartilage with ultra-short echo time (UTE) T2* mapping. Osteoarthr Cartil. 2010; 18:539–546. [PubMed: 20170769]
82. Reiter DA, Roque RA, Lin PC, et al. Mapping proteoglycan-bound water in cartilage: Improved specificity of matrix assessment using multiexponential transverse relaxation analysis. Magn Reson Med. 2011; 65:377–384. [PubMed: 21264931]
83. Aspden RM, Yarker YE, Hukins DW. Collagen orientations in the meniscus of the knee joint. J Anat. 1985; 140(Pt 3):371–380. [PubMed: 4066476]
84. Bullough PG, Munuera L, Murphy J, et al. The strength of the menisci of the knee as it relates to their fine structure. J Bone Joint Surg Br. 1970; 52:564–567. [PubMed: 5468789]

85. Skaggs DL, Warden WH, Mow VC. Radial tie fibers influence the tensile properties of the bovine medial meniscus. J Orthop Res. 1994; 12:176–185. [PubMed: 8164089]
86. Petersen W, Tillmann B. Collagenous fibril texture of the human knee joint menisci. Anatomy and embryology. 1998; 197:317–324. [PubMed: 9565324]
87. Kambic HE, McDevitt CA. Spatial organization of types I and II collagen in the canine meniscus. J Orthop Res. 2005; 23:142–149. [PubMed: 15607886]
88. McDevitt CA, Webber RJ. The ultrastructure and biochemistry of meniscal cartilage. Clin Orthop Relat Res. 1990:8–18. [PubMed: 2406077]
89. Arnoczky SP, Warren RF. Microvasculature of the human meniscus. Am J Sports Med. 1982; 10:90–95. [PubMed: 7081532]
90. Kean DM, Worthington BS, Preston BJ, et al. Nuclear magnetic resonance imaging of the knee: examples of normal anatomy and pathology. The British journal of radiology. 1983; 56:355–364. [PubMed: 6573932]
91. Berquist TH. Magnetic resonance imaging: preliminary experience in orthopedic radiology. Magnetic Resonance Imaging. 1984; 2:41–52. [PubMed: 6597880]
92. Li KC, Henkelman RM, Poon PY, et al. MR imaging of the normal knee. J Comput Assist Tomogr. 1984; 8:1147–1154. [PubMed: 6548762]
93. Crues JV 3rd, Mink J, Levy TL, et al. Meniscal tears of the knee: accuracy of MR imaging. Radiology. 1987; 164:445–448. [PubMed: 3602385]
94. Stoller DW, Martin C, Crues JV 3rd, et al. Meniscal tears: pathologic correlation with MR imaging. Radiology. 1987; 163:731–735. [PubMed: 3575724]
95. Hajek PC, Gylys-Morin VM, Baker LL, et al. The high signal intensity meniscus of the knee. Magnetic resonance evaluation and in vivo correlation. Invest Radiol. 1987; 22:883–890. [PubMed: 3429184]
96. Hodler J, Haghighi P, Pathria MN, et al. Meniscal changes in the elderly: correlation of MR imaging and histologic findings. Radiology. 1992; 184:221–225. [PubMed: 1609084]
97. Blackmon GB, Major NM, Helms CA. Comparison of fast spin-echo versus conventional spin-echo MRI for evaluating meniscal tears. AJR Am J Roentgenol. 2005; 184:1740–1743. [PubMed: 15908523]
98. Tarhan NC, Chung CB, Mohana-Borges AV, et al. Meniscal tears: role of axial MRI alone and in combination with other imaging planes. AJR Am J Roentgenol. 2004; 183:9–15. [PubMed: 15208100]
99. Kijowski R, Davis KW, Woods MA, et al. Knee joint: comprehensive assessment with 3D isotropic resolution fast spin-echo MR imaging--diagnostic performance compared with that of conventional MR imaging at 3.0 T. Radiology. 2009; 252:486–495. [PubMed: 19703886]
100. Eckstein F, Cicuttini F, Raynauld JP, et al. Magnetic resonance imaging (MRI) of articular cartilage in knee osteoarthritis (OA): morphological assessment. Osteoarthritis Cartilage. 2006; 14(A):A46–75. [PubMed: 16713720]
101. Potter HG, Black BR, Chong le R. New techniques in articular cartilage imaging. Clin Sports Med. 2009; 28:77–94. [PubMed: 19064167]
102. Bolbos RI, Link TM, Ma CB, et al. T1rho relaxation time of the meniscus and its relationship with T1rho of adjacent cartilage in knees with acute ACL injuries at 3 T. Osteoarthritis Cartilage. 2009; 17:12–18. [PubMed: 18602280]
103. Englund M, Guermazi A, Gale D, et al. Incidental meniscal findings on knee MRI in middle-aged and elderly persons. N Engl J Med. 2008; 359:1108–1115. [PubMed: 18784100]
104. Liess C, Lusse S, Karger N, et al. Detection of changes in cartilage water content using MRI T2-mapping in vivo. Osteoarthritis Cartilage. 2002; 10:907–913. [PubMed: 12464550]
105. Duvvuri U, Reddy R, Patel SD, et al. T1rho-relaxation in articular cartilage: effects of enzymatic degradation. Magn Reson Med. 1997; 38:863–867. [PubMed: 9402184]
106. Regatte RR, Akella SV, Wheaton AJ, et al. T 1 rho-relaxation mapping of human femoral-tibial cartilage in vivo. J Magn Reson Imaging. 2003; 18:336–341. [PubMed: 12938129]

107. Abreu M, Johnson K, Chung CB, et al. Calcification in calcium pyrophosphate dihydrate (CPPD) crystalline deposits in the knee: anatomic, radiographic, MR imaging, and histologic study in cadavers. Skeletal Radiol. 2004; 33:392–398. [PubMed: 15138720]
108. Beltran J, Marty-Delfaut E, Bencardino J, et al. Chondrocalcinosis of the hyaline cartilage of the knee: MRI manifestations. Skeletal Radiol. 1998; 27:369–374. [PubMed: 9730327]
109. Li X, Han ET, Busse RF, et al. In vivo T(1rho) mapping in cartilage using 3D magnetization-prepared angle-modulated partitioned k-space spoiled gradient echo snapshots (3D MAPSS). Magn Reson Med. 2008; 59:298–307. [PubMed: 18228578]
110. Bogduk, N.; Endres, SM. Clinical anatomy of the lumbar spine and sacrum. New York: Elsevier: Churchill Livingstone; 2005.
111. Marchand F, Ahmed AM. Investigation of the laminate structure of lumbar disc anulus fibrosus. Spine (Phila Pa 1976). 1990; 15:402–410. [PubMed: 2363068]
112. Cassidy JJ, Hiltner A, Baer E. Hierarchical structure of the intervertebral disc. Connect Tissue Res. 1989; 23:75–88. [PubMed: 2632144]
113. Veres SP, Robertson PA, Broom ND. The morphology of acute disc herniation: a clinically relevant model defining the role of flexion. Spine (Phila Pa 1976). 2009; 34:2288–2296. [PubMed: 19934808]
114. Buckwalter JA. Aging and degeneration of the human intervertebral disc. Spine. 1995; 20:1307–1314. [PubMed: 7660243]
115. Oegema TR Jr. Biochemistry of the intervertebral disc. Clin Sports Med. 1993; 12:419–439. [PubMed: 8364983]
116. Roughley PJ. Biology of intervertebral disc aging and degeneration: involvement of the extracellular matrix. Spine. 2004; 29:2691–2699. [PubMed: 15564918]
117. Setton LA, Zhu W, Weidenbaum M, et al. Compressive properties of the cartilaginous end-plate of the baboon lumbar spine. J Orthop Res. 1993; 11:228–239. [PubMed: 8483035]
118. Roberts S, Menage J, Urban JP. Biochemical and structural properties of the cartilage end-plate and its relation to the intervertebral disc. Spine. 1989; 14:166–174. [PubMed: 2922637]
119. Accadbled F, Laffosse JM, Ambard D, et al. Influence of location, fluid flow direction, and tissue maturity on the macroscopic permeability of vertebral end plates. Spine (Phila Pa 1976). 2008; 33:612–619. [PubMed: 18344854]
120. Crock HV, Goldwasser M. Anatomic Studies of the Circulation in the Region of the Vertebral End-Plate in Adult Greyhound Dogs. Spine. 1984; 9:702–706. [PubMed: 6505840]
121. Brodin H. Paths of nutrition in articular cartilage and intervertebral discs. Acta Orthop Scand. 1955; 24:177–183. [PubMed: 14387660]
122. Urban JP, Holm S, Maroudas A. Diffusion of small solutes into the intervertebral disc: as in vivo study. Biorheology. 1978; 15:203–221. [PubMed: 737323]
123. Urban JP, Holm S, Maroudas A, et al. Nutrition of the intervertebral disc: effect of fluid flow on solute transport. Clin Orthop Rel Res. 1982; 170:296–306.
124. Maroudas A, Stockwell RA, Nachemson A, et al. Factors involved in the nutrition of the human lumbar intervertebral disc: cellularity and diffusion of glucose in vitro. J Anat. 1975; 120:113–130. [PubMed: 1184452]
125. Roberts S, Menage J, Eisenstein SM. The cartilage end-plate and intervertebral disc in scoliosis: calcification and other sequelae. J Orthop Res. 1993; 11:747–757. [PubMed: 8410475]
126. Urban MR, Fairbank JC, Etherington PJ, et al. Electrochemical measurement of transport into scoliotic intervertebral discs in vivo using nitrous oxide as a tracer. Spine. 2001; 26:984–990. [PubMed: 11317125]
127. Andersson GB. Epidemiological features of chronic low-back pain. Lancet. 1999; 354:581–585. [PubMed: 10470716]
128. An HS, Anderson PA, Haughton VM, et al. Introduction: disc degeneration: summary. Spine. 2004; 29:2677–2678. [PubMed: 15564916]
129. Kawakami M, Tamaki T, Hayashi N, et al. Possible mechanism of painful radiculopathy in lumbar disc herniation. Clin Orthop Relat Res. 1998:241–251. [PubMed: 9646768]

130. Moneta GB, Videman T, Kaivanto K, et al. Reported pain during lumbar discography as a function of anular ruptures and disc degeneration. A re-analysis of 833 discograms. Spine (Phila Pa 1976). 1994; 19:1968–1974. [PubMed: 7997931]
131. Vanharanta H, Sachs BL, Spivey MA, et al. The relationship of pain provocation to lumbar disc deterioration as seen by CT/discography. Spine (Phila Pa 1976). 1987; 12:295–298. [PubMed: 3589823]
132. Powell MC, Wilson M, Szypryt P, et al. Prevalence of lumbar disc degeneration observed by magnetic resonance in symptomless women. Lancet. 1986; 2:1366–1367. [PubMed: 2878228]
133. Boden SD, Davis DO, Dina TS, et al. Abnormal magnetic-resonance scans of the lumbar spine in asymptomatic subjects. A prospective investigation. J Bone Joint Surg Am. 1990; 72:403–408. [PubMed: 2312537]
134. Bernick S, Cailliet R. Vertebral end-plate changes with aging of human vertebrae. Spine (Phila Pa 1976). 1982; 7:97–102. [PubMed: 7089697]
135. Nachemson A, Lewin T, Maroudas A, et al. In vitro diffusion of dye through the end-plates and the annulus fibrosus of human lumbar inter-vertebral discs. Acta Orthop Scand. 1970; 41:589–607. [PubMed: 5516549]
136. Aigner T, Gresk-otter KR, Fairbank JC, et al. Variation with age in the pattern of type × collagen expression in normal and scoliotic human intervertebral discs. Calcif Tissue Int. 1998; 63:263–268. [PubMed: 9701632]
137. van der Werf M, Lezuo P, Maissen O, et al. Inhibition of vertebral endplate perfusion results in decreased intervertebral disc intranuclear diffusive transport. J Anat. 2007; 211:769–774. [PubMed: 17953653]
138. Forristall RM, Marsh HO, Pay NT. Magnetic resonance imaging and contrast CT of the lumbar spine. Comparison of diagnostic methods and correlation with surgical findings. Spine (Phila Pa 1976). 1988; 13:1049–1054. [PubMed: 3206299]
139. Hashimoto K, Akahori O, Kitano K, et al. Magnetic resonance imaging of lumbar disc herniation. Comparison with myelography. Spine (Phila Pa 1976). 1990; 15:1166–1169. [PubMed: 2267612]
140. Pearce RH, Thompson JP, Bebault GM, et al. Magnetic resonance imaging reflects the chemical changes of aging degeneration in the human intervertebral disk. J Rheumatol Suppl. 1991; 27:42–43. [PubMed: 2027127]
141. Pfirrmann CW, Metzdorf A, Zanetti M, et al. Magnetic resonance classification of lumbar intervertebral disc degeneration. Spine. 2001; 26:1873–1878. [PubMed: 11568697]
142. Masuda K, Imai Y, Okuma M, et al. Osteogenic protein-1 injection into a degenerated disc induces the restoration of disc height and structural changes in the rabbit anular puncture model. Spine. 2006; 31:742–754. [PubMed: 16582847]
143. Lee S, Moon CS, Sul D, et al. Comparison of growth factor and cytokine expression in patients with degenerated disc disease and herniated nucleus pulposus. Clin Biochem. 2009; 42:1504–1511. [PubMed: 19563795]
144. Pfirrmann CW, Metzdorf A, Elfering A, et al. Effect of aging and degeneration on disc volume and shape: A quantitative study in asymptomatic volunteers. J Orthop Res. 2006; 24:1086–1094. [PubMed: 16609964]
145. Rajasekaran S, Babu JN, Arun R, et al. ISSLS prize winner: A study of diffusion in human lumbar discs: a serial magnetic resonance imaging study documenting the influence of the endplate on diffusion in normal and degenerate discs. Spine (Phila Pa 1976). 2004; 29:2654–2667. [PubMed: 15564914]
146. Antoniou J, Goudsouzian NM, Heathfield TF, et al. The human lumbar endplate. Evidence of changes in biosynthesis and denaturation of the extracellular matrix with growth, maturation, aging, and degeneration. Spine (Phila Pa 1976). 1996; 21:1153–1161. [PubMed: 8727189]
147. Marinelli NL, Haughton VM, Munoz A, et al. T2 relaxation times of intervertebral disc tissue correlated with water content and proteoglycan content. Spine (Phila Pa 1976). 2009; 34:520–524. [PubMed: 19247172]
148. Panagiotacopulos ND, Pope MH, Krag MH, et al. Water content in human intervertebral discs. Part I. Measurement by magnetic resonance imaging. Spine (Phila Pa 1976). 1987; 12:912–917. [PubMed: 3441837]

149. Chatani K, Kusaka Y, Mifune T, et al. Topographic differences of 1H-NMR relaxation times (T1, T2) in the normal intervertebral disc and its relationship to water content. Spine (Phila Pa 1976). 1993; 18:2271–2275. [PubMed: 8278845]

150. Kerttula L, Kurunlahti M, Jauhiainen J, et al. Apparent diffusion coefficients and T2 relaxation time measurements to evaluate disc degeneration. A quantitative MR study of young patients with previous vertebral fracture. Acta Radiol. 2001; 42:585–591. [PubMed: 11736706]

151. Karakida O, Ueda H, Ueda M, et al. Diurnal T2 value changes in the lumbar intervertebral discs. Clin Radiol. 2003; 58:389–392. [PubMed: 12727168]

152. Ludescher B, Effelsberg J, Martirosian P, et al. T2- and diffusion-maps reveal diurnal changes of intervertebral disc composition: an in vivo MRI study at 1.5 Tesla. J Magn Reson Imaging. 2008; 28:252–257. [PubMed: 18581387]

153. Benneker LM, Heini PF, Anderson SE, et al. Correlation of radiographic and MRI parameters to morphological and biochemical assessment of intervertebral disc degeneration. Eur Spine J. 2005; 14:27–35. [PubMed: 15723249]

154. Buck FM, Bae WC, Diaz E, et al. Comparison of T1rho measurements in agarose phantoms and human patellar cartilage using 2D multislice spiral and 3D magnetization prepared partitioned k-space spoiled gradient-echo snapshot techniques at 3 T. AJR Am J Roentgenol. 2011; 196:W174–179. [PubMed: 21257859]

155. Drew SC, Silva P, Crozier S, et al. A diffusion and T2 relaxation MRI study of the ovine lumbar intervertebral disc under compression in vitro. Phys Med Biol. 2004; 49:3585–3592. [PubMed: 15446789]

156. Majumdar S. Magnetic resonance imaging and spectroscopy of the intervertebral disc. NMR Biomed. 2006; 19:894–903. [PubMed: 17075964]

157. Zuo J, Saadat E, Romero A, et al. Assessment of intervertebral disc degeneration with magnetic resonance single-voxel spectroscopy. Magn Reson Med. 2009

158. Keshari KR, Lotz JC, Link TM, et al. Lactic acid and proteoglycans as metabolic markers for discogenic back pain. Spine (Phila Pa 1976). 2008; 33:312–317. [PubMed: 18303465]

159. Xia Y. Magic-angle effect in magnetic resonance imaging of articular cartilage: a review. Invest Radiol. 2000; 35:602–621. [PubMed: 11041155]

160. Szeverenyi NM, Bydder GM. Dipolar anisotropy fiber imaging in a goat knee meniscus. Magn Reson Med. 2010

161. Bae WC, Statum S, Znamirowski R, et al. Dipolar Anisotropy Fiber Imaging of Human Anulus Fibrosus. Proc Int'l Soc Magn Reson Med. 2011; 19:2569.

162. Bae WC, Xu K, Inoue N, et al. Ultrashort time-to-echo MRI of human intervertebral disc endplate: association with endplate calcification. Proc Int'l Soc Magn Reson Med. 2010; 18:3218.

163. Bae WC, Yoshikawa T, Hemmad AR, et al. Ultrashort time-to-echo MRI of human intervertebral disc endplate: association with disc degeneration. Proc Int'l Soc Magn Reson Med. 2010; 18:534.

164. Gatehouse PD, He T, Hughes SP, et al. MR imaging of degenerative disc disease in the lumbar spine with ultrashort TE pulse sequences. Magma. 2004; 16:160–166. [PubMed: 14986145]

165. Masuda K, Oegema TR Jr, An HS. Growth factors and treatment of intervertebral disc degeneration. Spine. 2004; 29:2757–2769. [PubMed: 15564925]

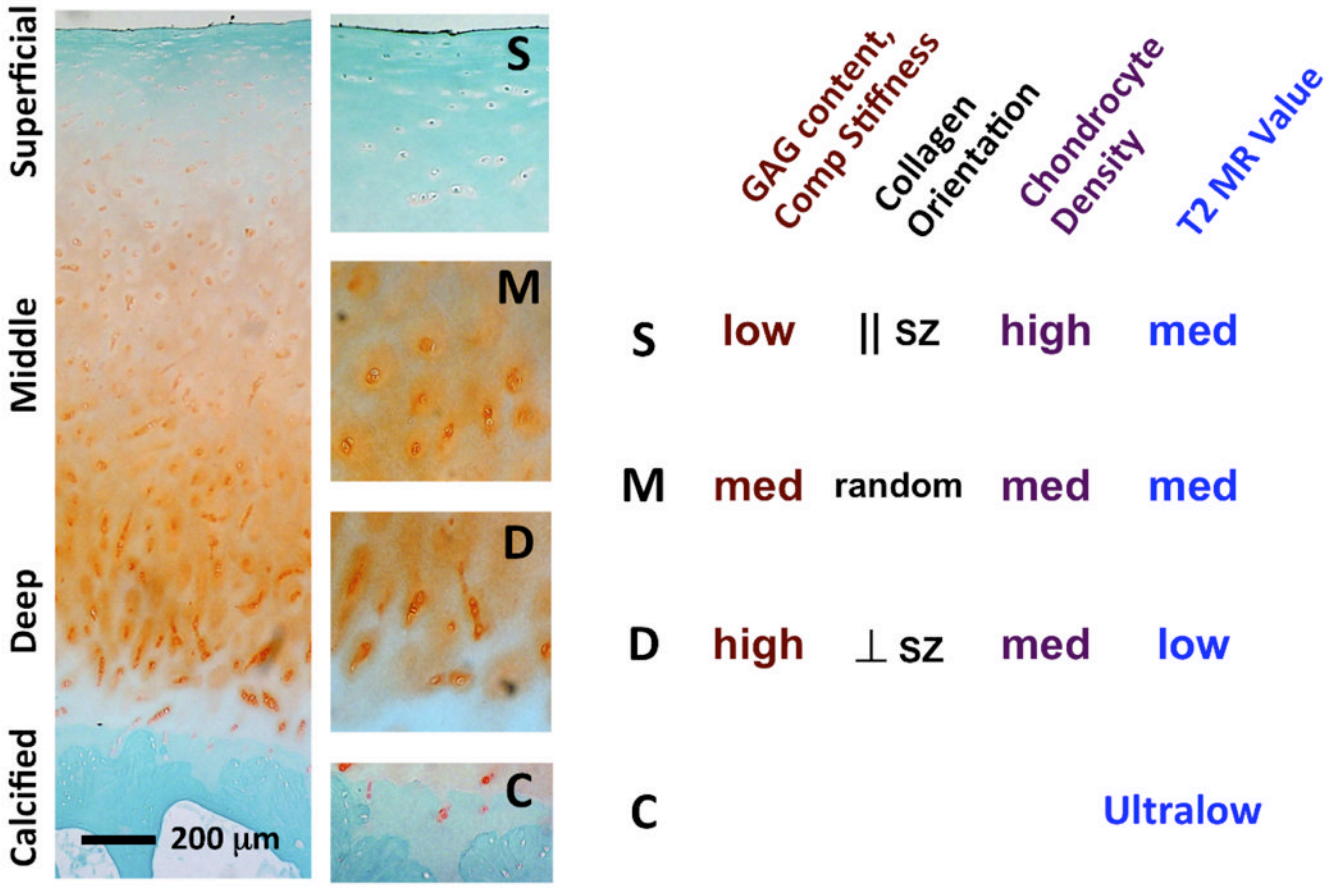

Figure 1.

(**left**) Paraffin histology of articular cartilage from femoral condyle stained with Safranin-O and fast green; magnified sections from superficial, middle, deep and calcified layers are also shown. (**right**) depth-variations in glycosaminoglycan content, compressive stiffness, collagen fibril orientation, chondrocyte density and T2 values.

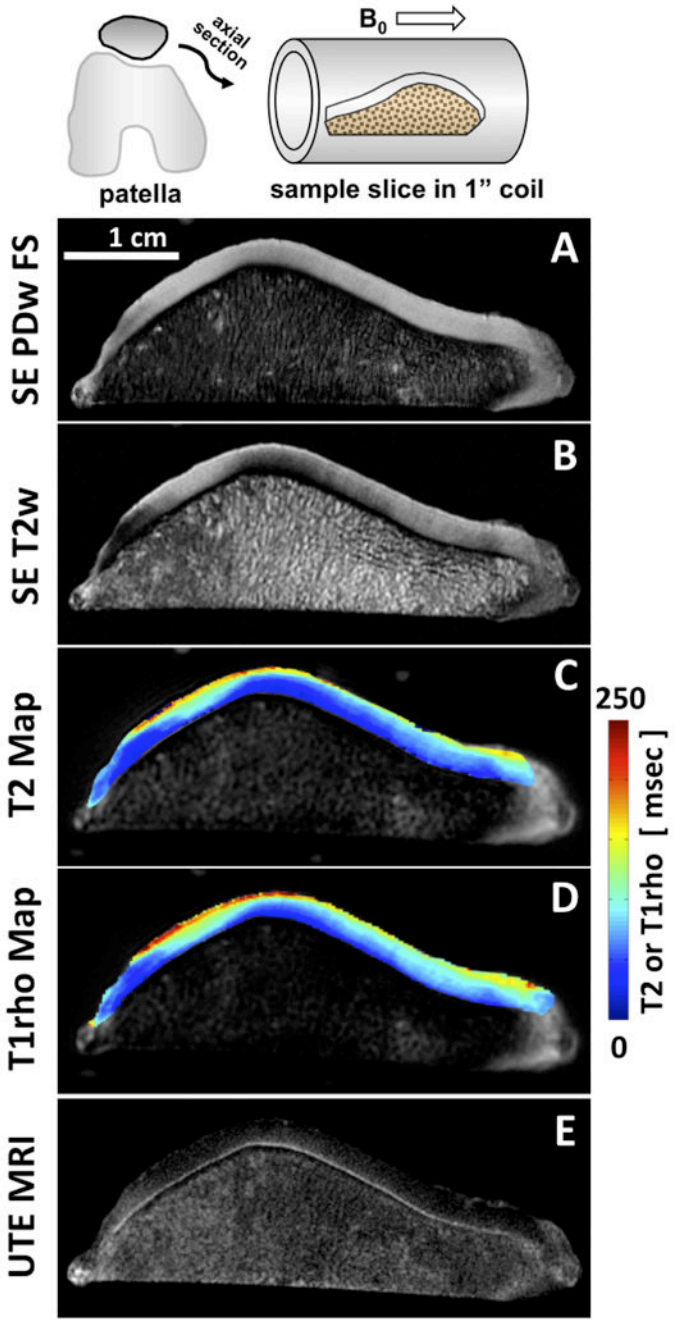

Figure 2.

Conventional and UTE MRI of a human patella slice. Conventional spin echo (**A**) proton density-weighted fat suppressed and (**B**) intermediate T2-weighted images are often used for clinical evaluation. Conventional quantitative (**C**) T2 and (**D**) T1rho mapping techniques are clinically-applicable and yield continuous data that can be compared to metrics more efficiently. Unlike the conventional techniques, UTE MRI echo subtraction image (**E**) reveals the deepest layer of articular cartilage with linear high signal intensity.

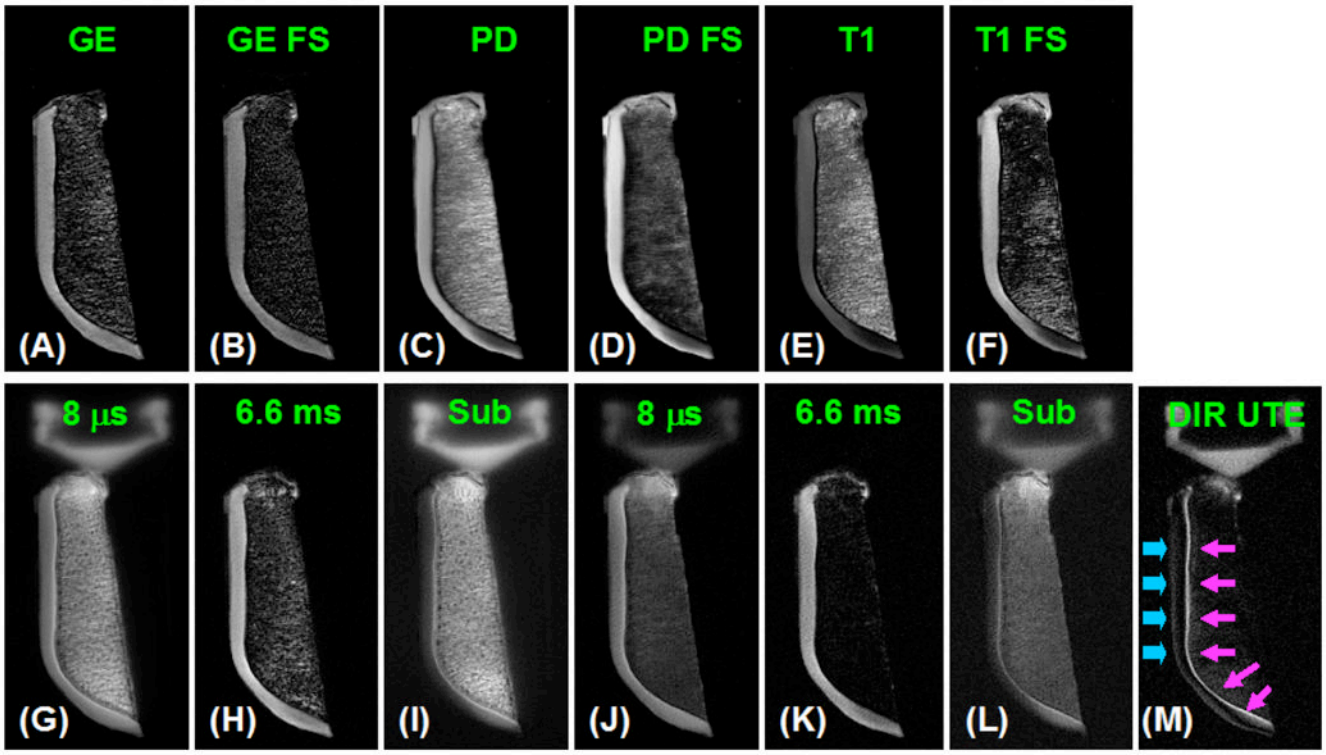

Figure 3.

Axial imaging of a patella slice with clinical gradient echo (**A**), GE with fat saturation (**B**), PD FSE (**C**), PD FSE with FS (**D**), T1 FSE (**E**), T1 FSE with FS (**F**), conventional UTE with a TE of 8 μs (**G**) and 6.6 ms (**H**), subtraction of the second echo from the first echo (**I**), fat saturated UTE with a TE of 8 μs (**J**) and 6.6 ms (**K**) with the corresponding later echo subtraction (**L**), and DIR UTE (**M**). Clinical gradient echo or spin echo sequences show no signal from the calcified cartilage, which appears bright with UTE sequences but there is limited contrast between the deep layers of cartilage and superficial layers of cartilage as well as with bone marrow fat. The DIR UTE image shows the calcified cartilage with excellent contrast (pink arrows) with good suppression of the superficial layers of cartilage and fat. There is some signal from the superficial layer of cartilage due to variation in T1.

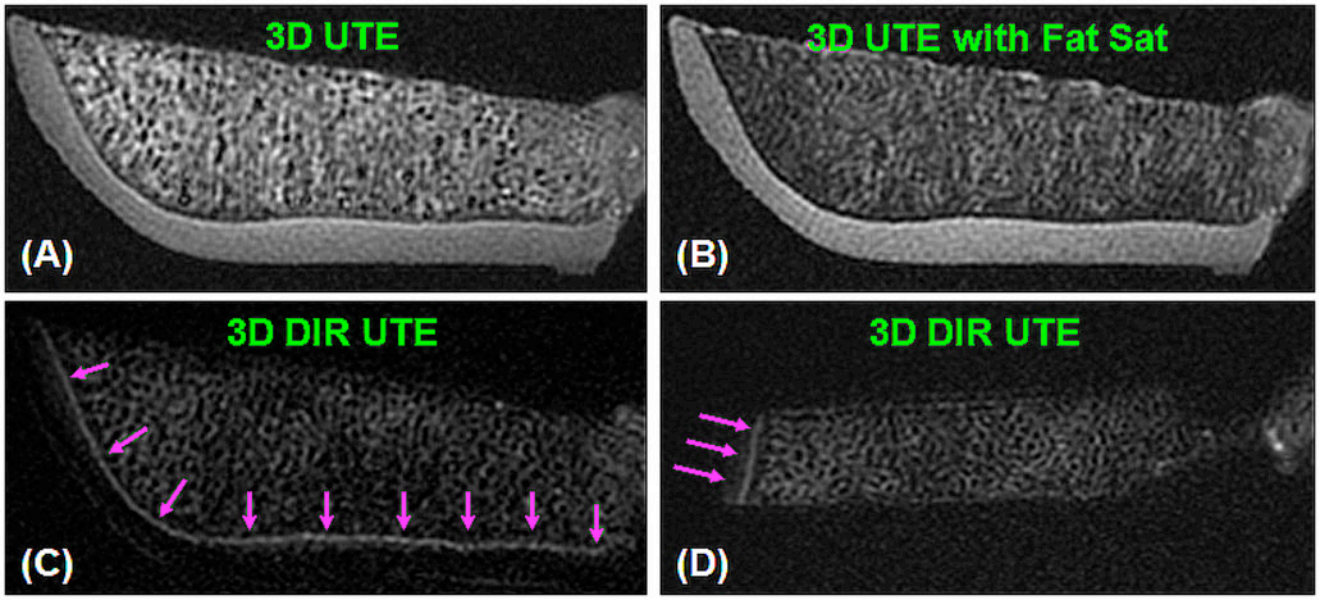

Figure 4.

Axial imaging of a patellar slice using regular 3D UTE (**A**), 3D UTE with fat saturation (**B**), and 3D DIR UTE in the axial (**C**) and sagittal (**D**) reprojections. Regular 3D UTE without or with fat saturation pulse provides high signal but limited contrast for the calcified cartilage. The 3D DIR UTE sequence selectively suppresses signals from the superficial layers of cartilage and bone marrow fat, creating excellent contrast for the calcified cartilage (arrows) with an isotropic resolution of $0.16\times0.16\times0.16\ mm^3$.

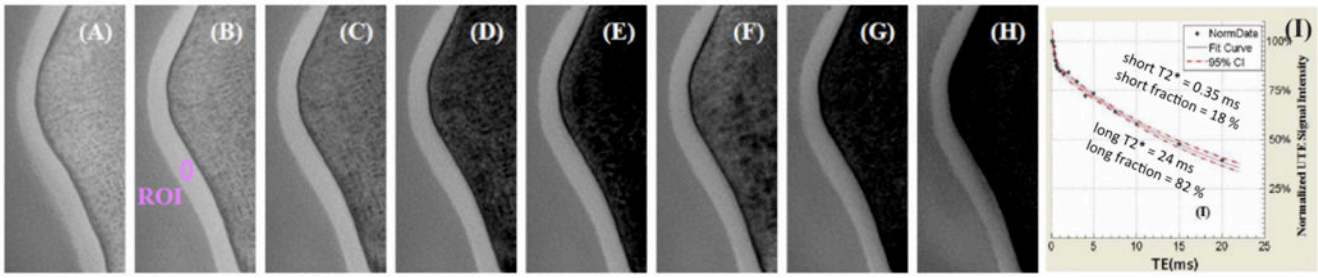

Figure 5.

UTE MR imaging of cadaveric patellar cartilage and bi-component analysis. The following parameters were used: TR = 500 ms, FOV = 10 cm, slice thickness = 2 mm, reconstruction matrix = 512 × 512, 17 TEs ranging from 8 μs to 20 ms (every other TE shown in **A to H**). (**I**) A bi-component analysis of the patellar cartilage yielded short and long T2* values as well as their fractions.

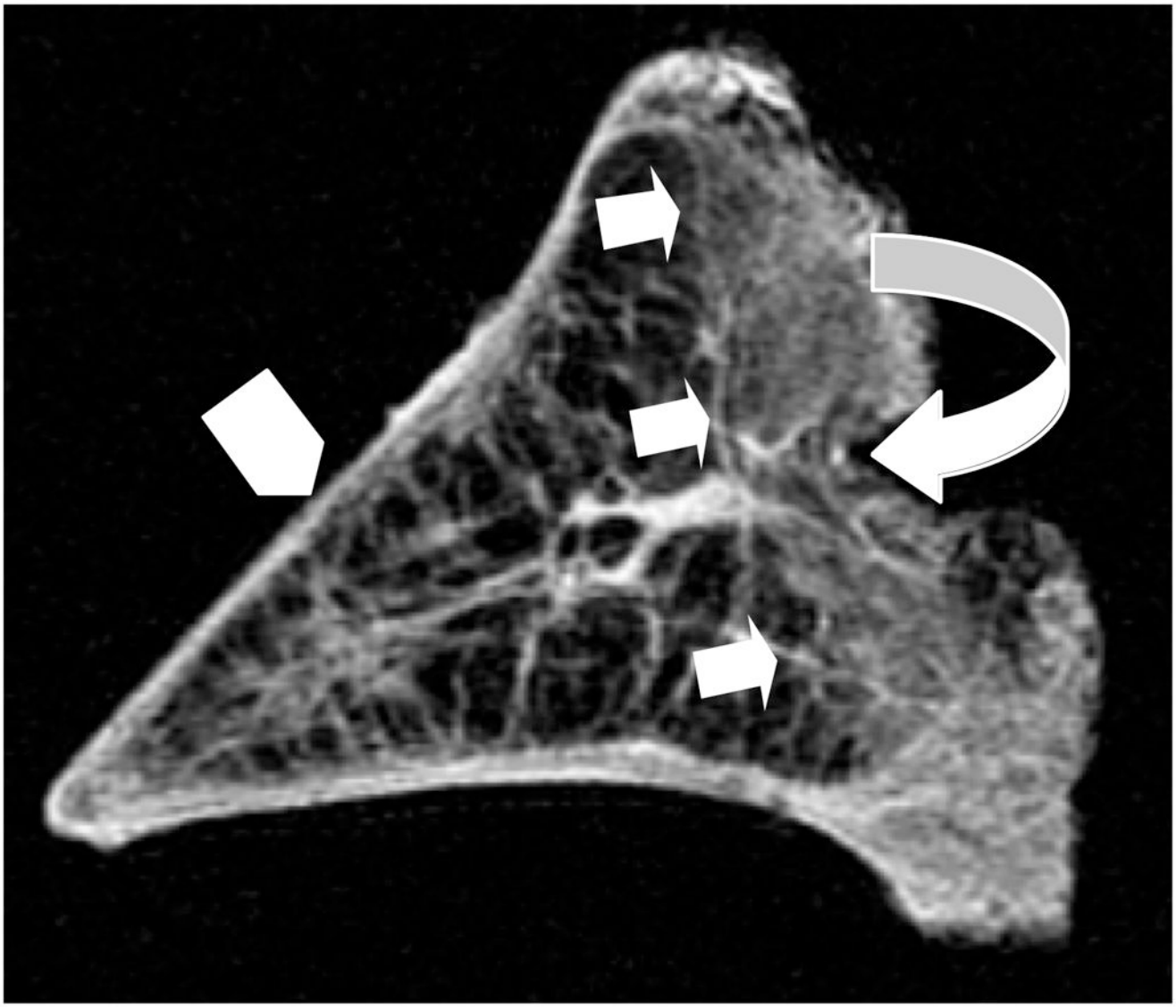

Figure 6.
Short TE MR image of a sagittal section of meniscal tissue demonstrates the identification of the posterior red zone (curved arrow) and its well-defined delineation (straight arrows) from the more central white zone (arrowhead).

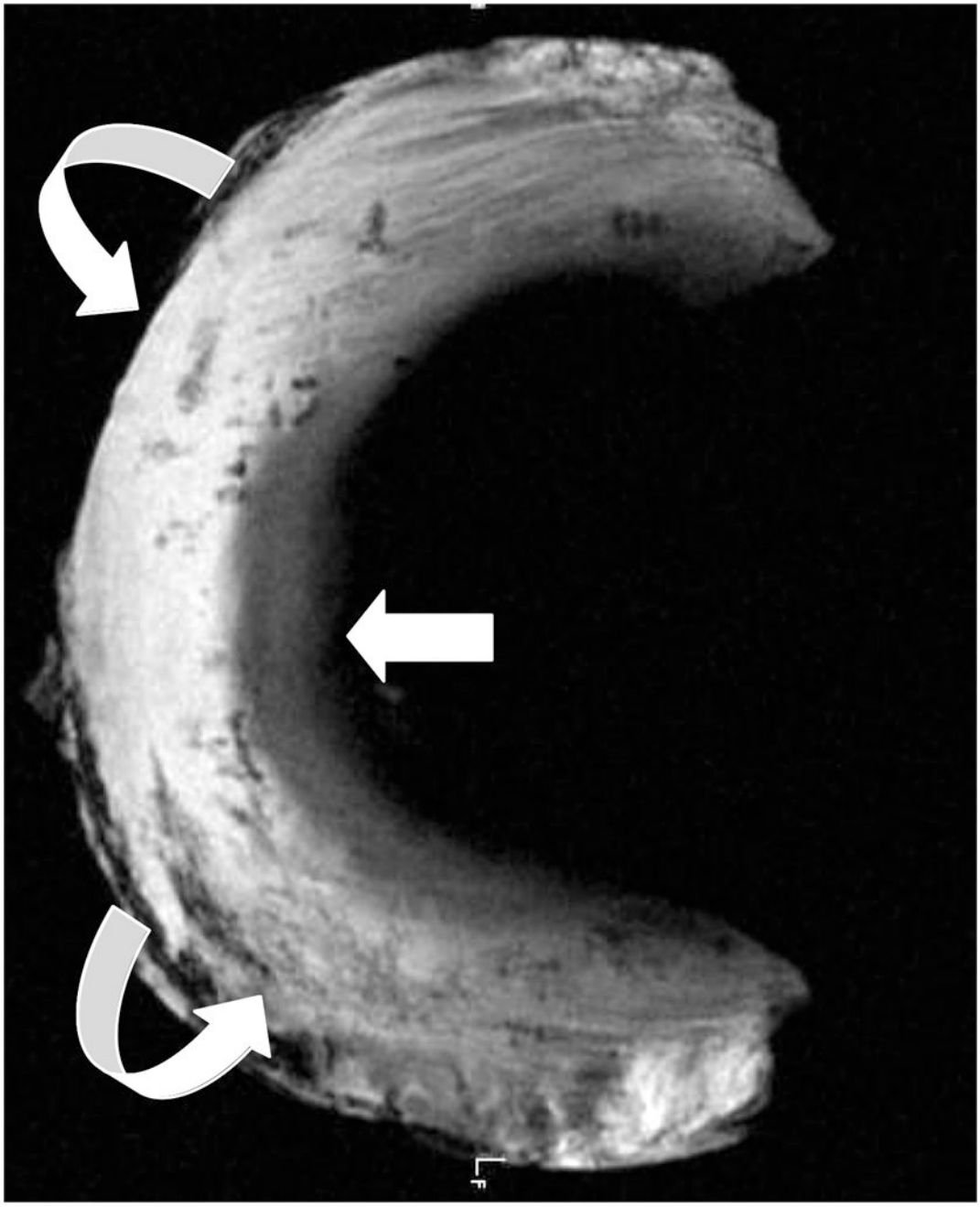

Figure 7.
Axial UTE MR image through human meniscal tissue shows its inner cartilaginous component with intermediate signal intensity, whereas the peripheral more fibrous composition (curved arrows) of the tissue results in higher signal.

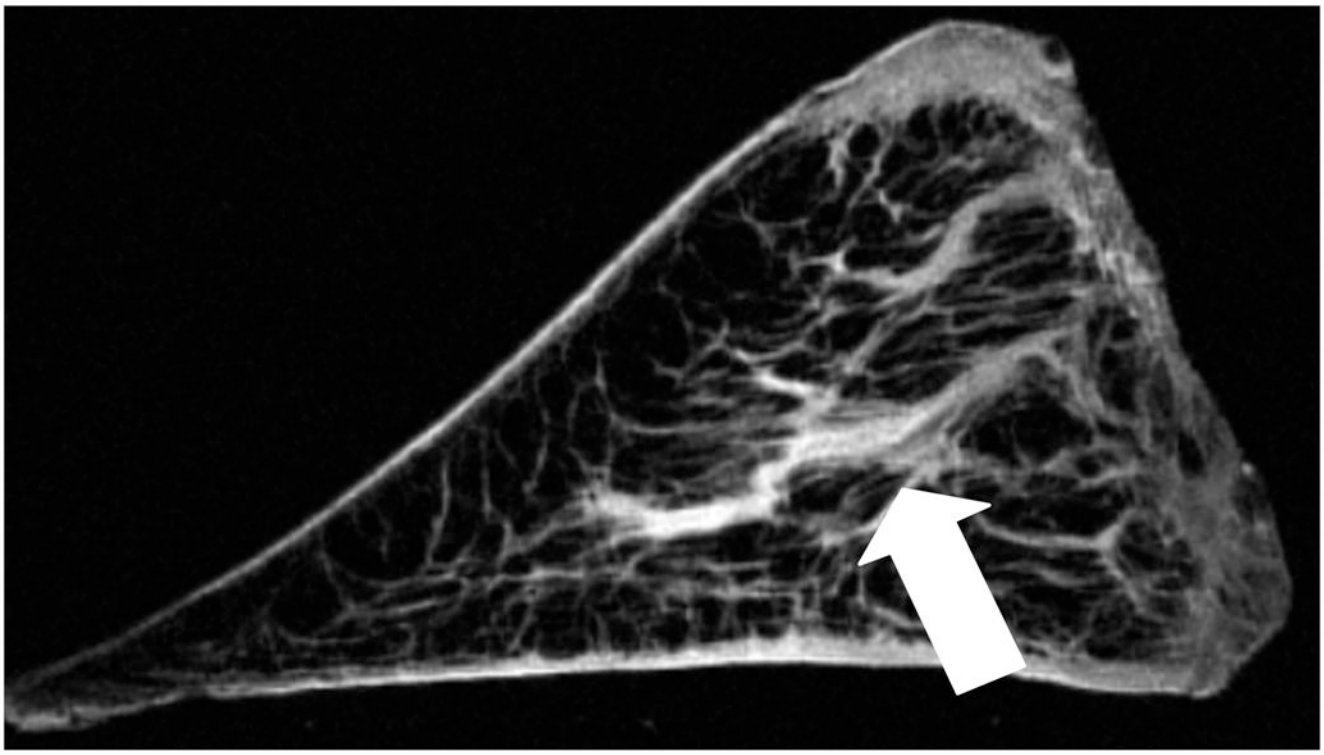

Figure 8.
Sagittal short TE MR image through human meniscal tissue shows a dominant radial fiber (arrow) extending from the peripheral margin into the white zone.

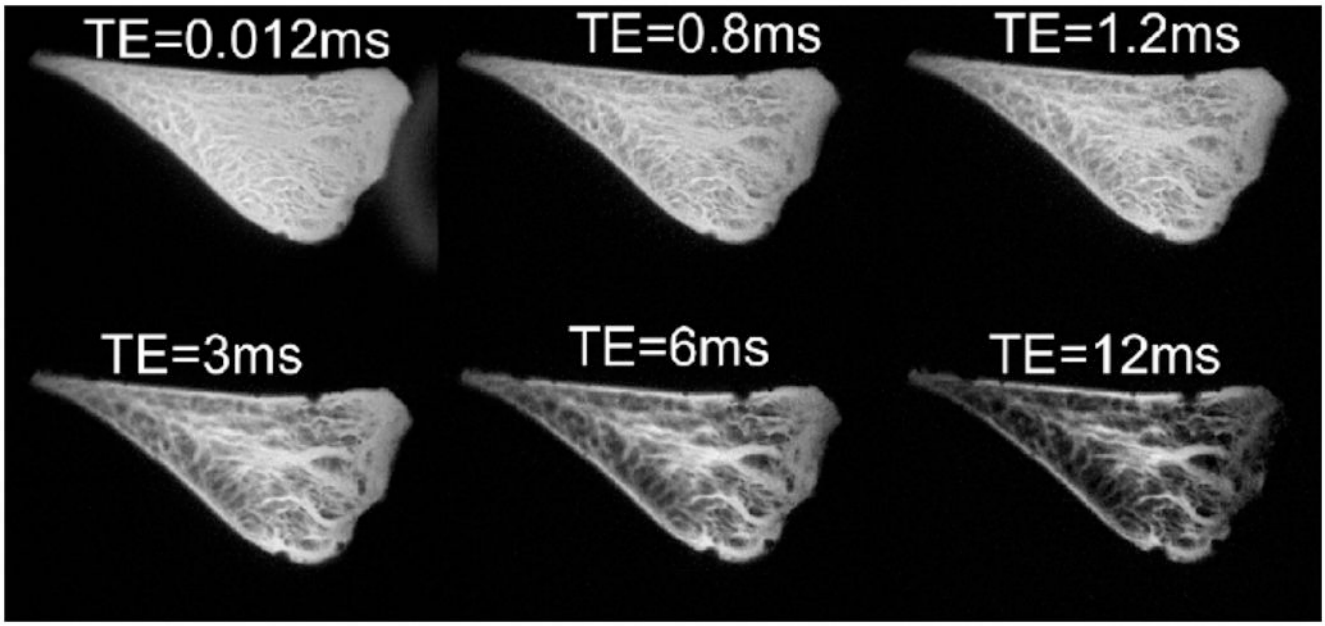

Figure 9.
Sagittal fat saturated UTE MR images of cadaveric menisci with varying TEs (0.012 to 12 ms). Fibrocartilage is best depicted at lowest TEs, while the fibrillar network is better shown at TE ~5 ms.

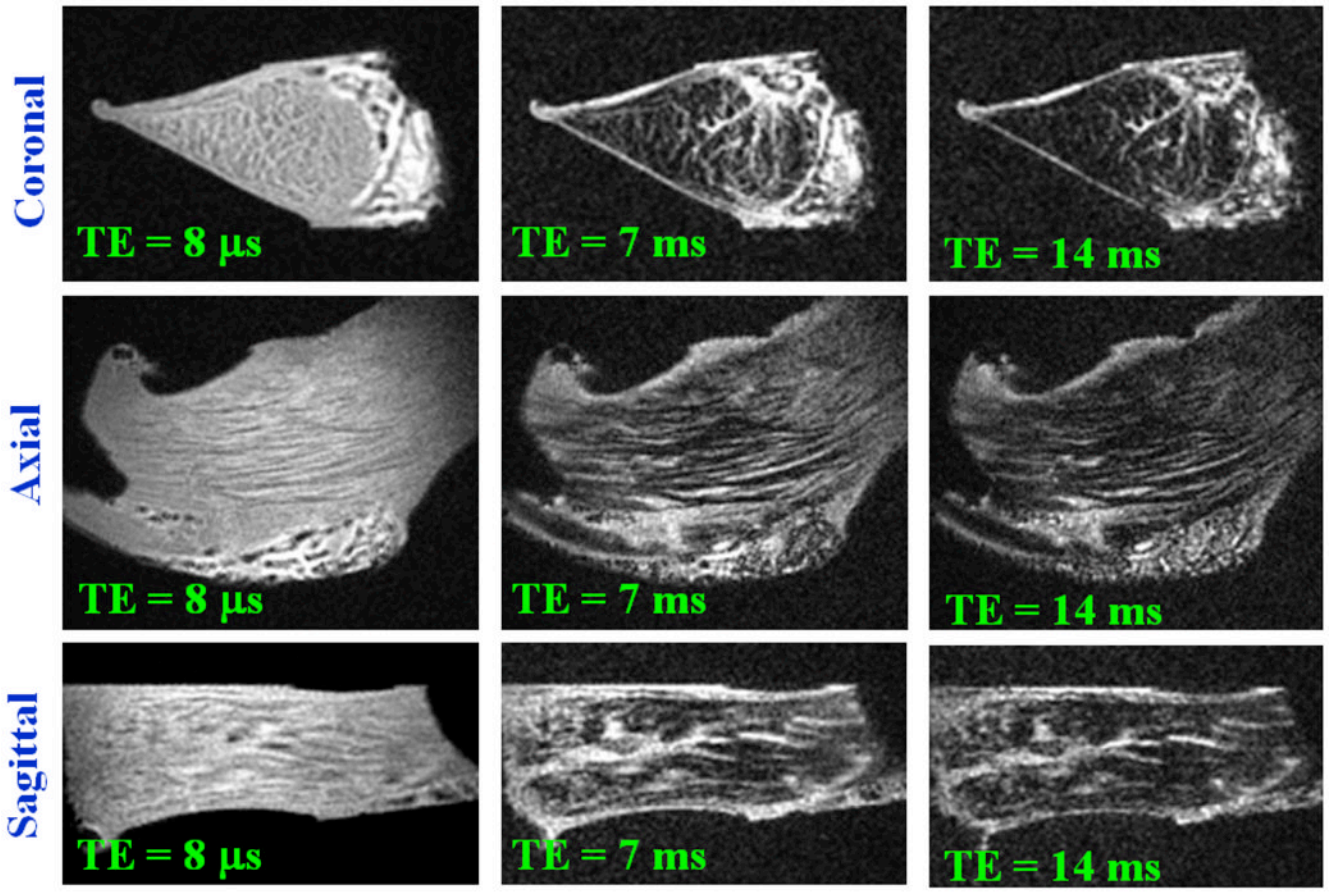

Figure 10.
Cadaveric meniscus imaged using isotropic 3D UTE technique. Three anatomic planes are shown at varying TEs.

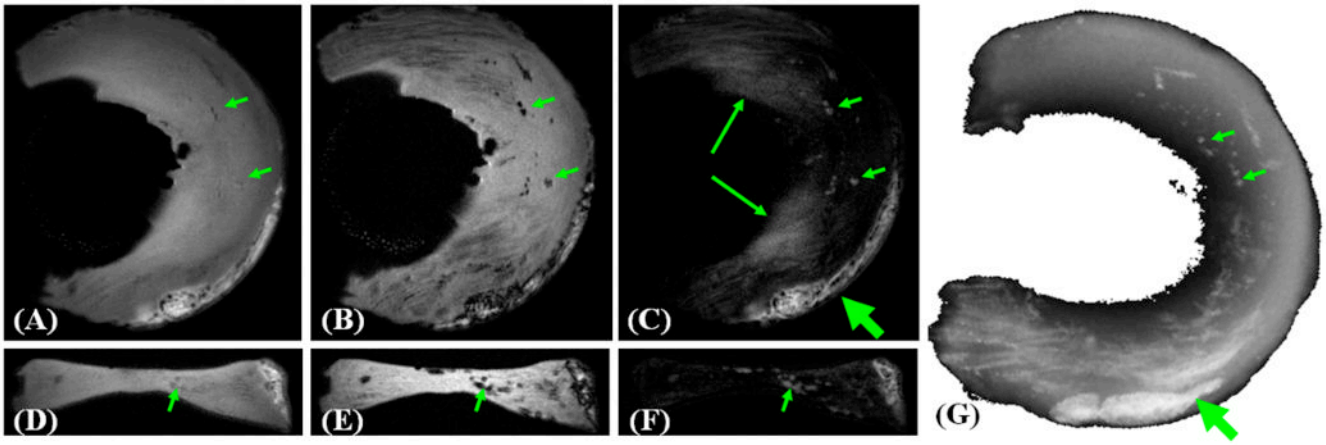

Figure 11.

Dual echo 3D UTE imaging of meniscal calcification in the coronal (**A, B**) and axial plane (**D, E**). Meniscal calcification is depicted with high contrast and isotropic spatial resolution (short arrows) in the corresponding subtraction images (**C, F**), which correlate well with x-ray image (**G**). There is some residual signal from fat (thick arrows) and meniscal regions (long arrows) which experienced significant signal decay between the first and second echoes, and appeared as high signal on the subtraction image.

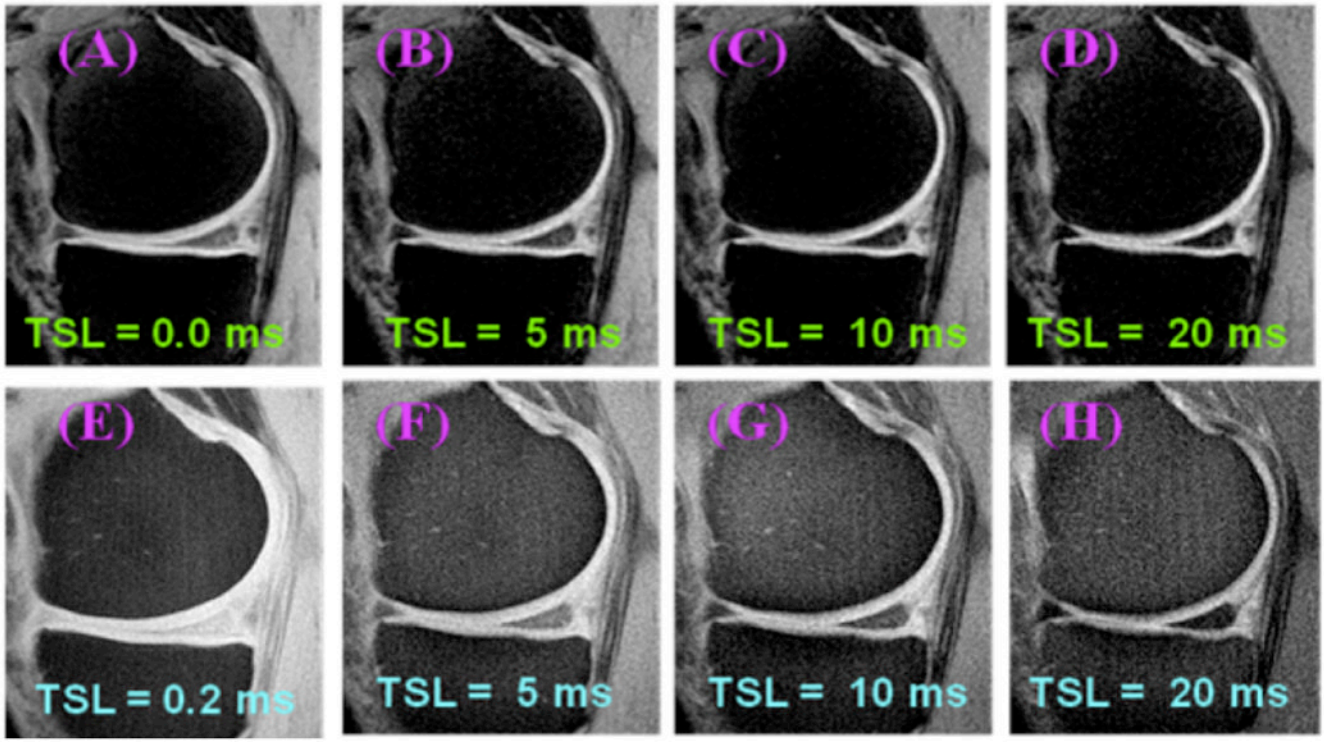

Figure 12.

T1ρ imaging using MAPSS (**A-D**) and UTE T1rho (**E-H**), as well as single component T1rho fitting based on MAPSS and UTE T1rho imaging (**I**). UTE T1rho imaging provides significantly shorter T1rho value of 8.56 ± 1.01 ms, as compared to 12.51 ± 1.18 ms fitted from MAPSS imaging.

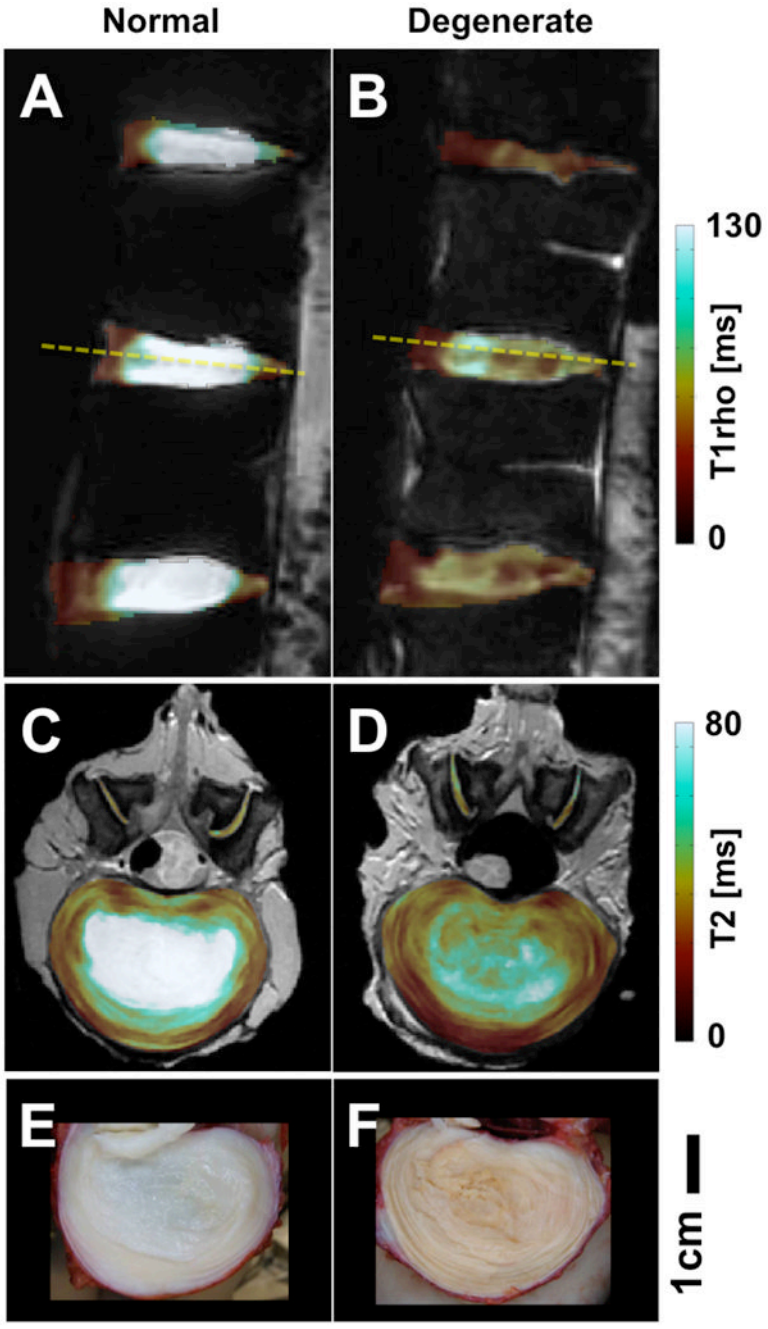

Figure 13.
Conventional MRI targeting tissues with long T2s. (**A,C,E**) normal and (**B,D,F**) degenerate lumbar discs. (**A,B**) T1rho maps, (**C,D**) T2 maps and (**E,F**) gross photos.

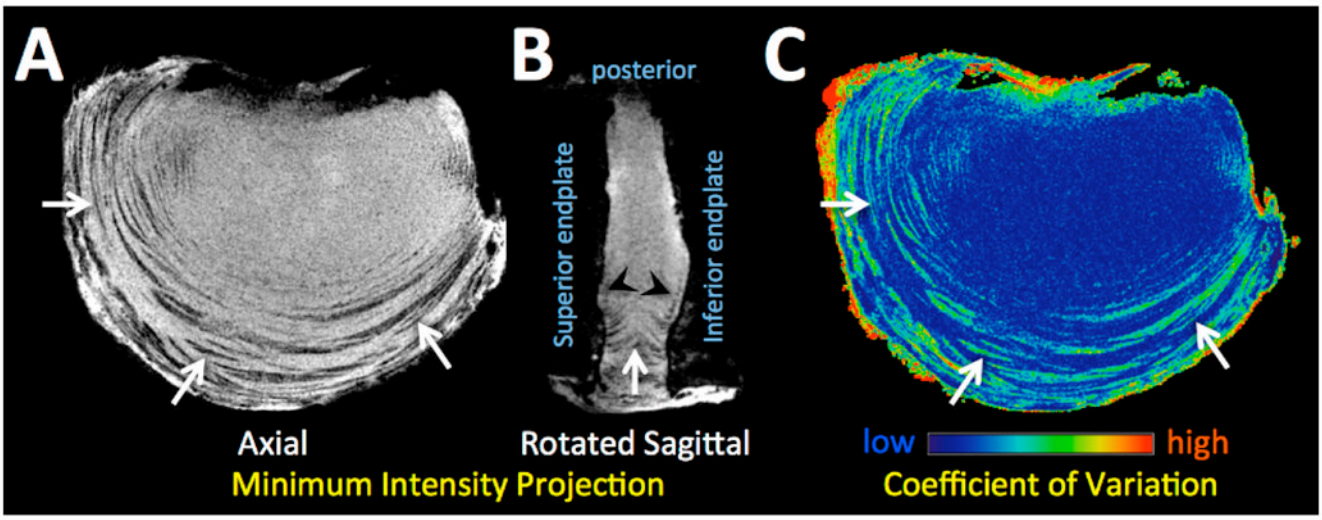

Figure 14.

Short TE gradient echo MR images of the sample in multiple orientation were processed to create a minimum intensity projection images in the (**A**) axial and (**B**) mid-sagittal planes, showing the AF lamellae as dark bands with a high contrast against surrounding matrices. (**C**) The AF lamellae exhibited high coefficients of variations, as expected for structures experiencing the magic angle effect.

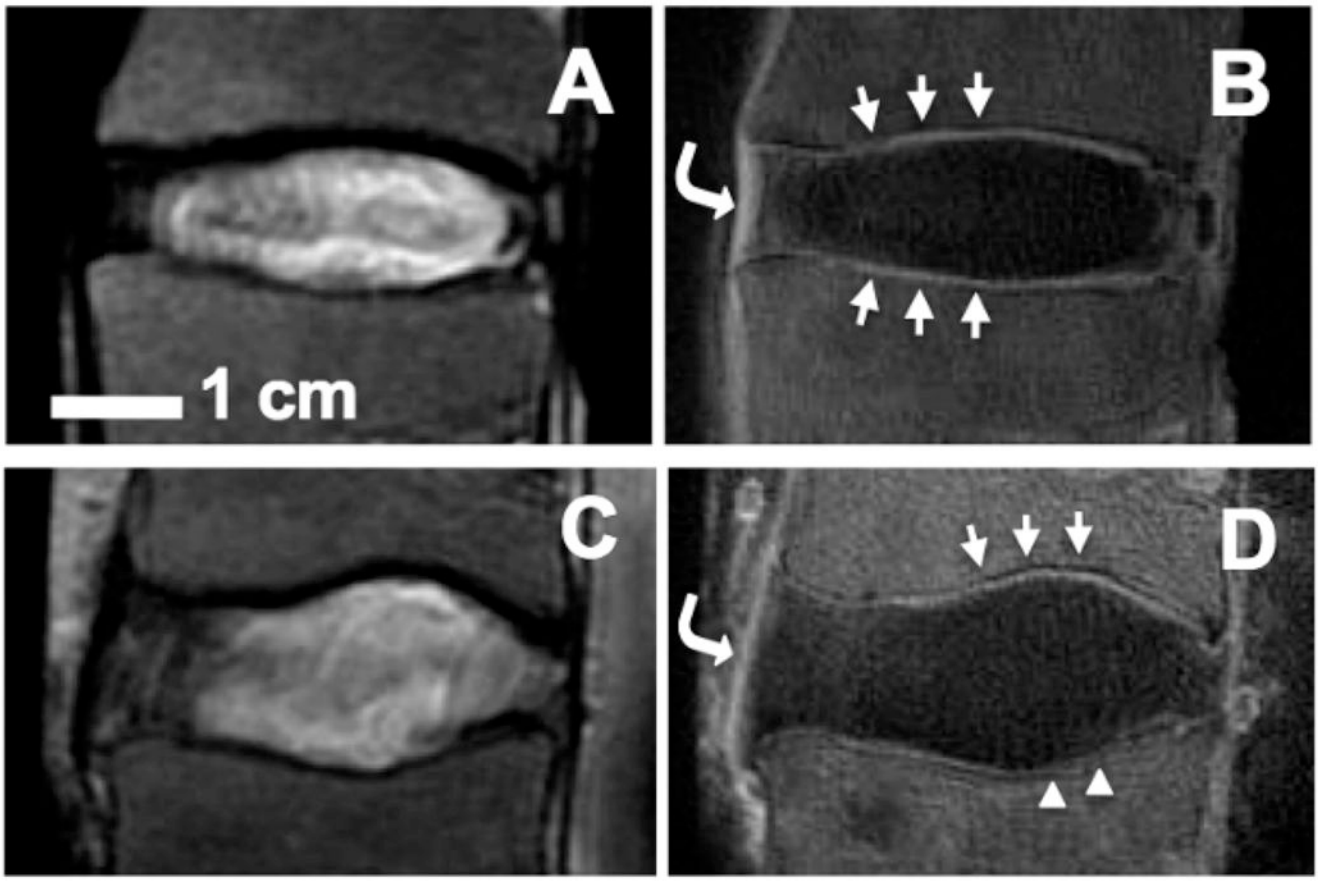

Figure 15.
UTE MRI appearance of normal human spine segments. (**A,B**) T2-weighted spin echo MRI shows relatively normal discs and vertebral body. Region of cartilaginous endplate (CEP) appears dark. (**B**) Normal appearance of CEP in UTE MRI. Note characteristic high-intensity linear signal (arrows). (**D**) Abnormal appearance of CEP in UTE MRI. Note focally-diminished signal on the caudal CEP (triangles). In UTE MR images (**B,D**), longitudinal ligaments (curved arrows) are visible. Bar=1 cm.